Lappalainen, Jari; Hakkarainen, Elina; Sihvonen, Teemu; Rodríguez-García, Margarita M.; Alopaeus, Ville

Modelling a molten salt thermal energy system – A validation study

Published in:
Applied Energy

DOI:
10.1016/j.apenergy.2018.10.009

Published: 01/01/2019

Document Version
Publisher's PDF, also known as Version of record

Applied Energy 233–234 (2019) 126–145

Contents lists available at ScienceDirect

Applied Energy

journal homepage: www.elsevier.com/locate/apenergy

Modelling a molten salt thermal energy system – A validation study

Jari Lappalainen[a,*], Elina Hakkarainen[a], Teemu Sihvonen[b], Margarita M. Rodríguez-García[c], Ville Alopaeus[d]

[a] VTT Technical Research Centre of Finland Ltd, Vuorimiehentie 3, 02044 Espoo, Finland
[b] VTT Technical Research Centre of Finland Ltd, Koivurannantie 1, 40400 Jyväskylä, Finland
[c] CIEMAT-Plataforma Solar de Almería, Carretera de Senés, km 4, 04200 Tabernas, Almería, Spain
[d] Aalto University, Department of Biotechnology and Chemical Technology, 02150 Espoo, Finland

HIGHLIGHTS

- Easily define a mixture of molten salt and non-condensable gas for rigorous dynamic simulation.
- Enables system-wide thermal and hydrodynamic analysis for energy storage processes.
- New experimental data on operating a thermal energy storage facility using molten salt.
- The heat exchanger performance is influenced by trapped non-condensable gas.
- Anomalous sudden changes in the hydrodynamic losses uncovered.

ARTICLE INFO

Keywords:
Dynamic simulation
Thermal hydraulics
Molten salt
Heat exchanger
Thermal energy storage
Concentrated solar power

ABSTRACT

Thermal energy storage (TES) plays a crucial role improving the efficiency of solar power utilization. Molten salt (MS) has gained a strong position as a thermal fluid in applications where solar power is stored and used overnight to provide dispatchable energy production. Novel process and operating concepts are being developed for TES systems that require reliable engineering tools. System-wide dynamic simulation provides a virtual test bench and analysis tool for assisting in process and control design and operational issues. Proper characterization of the thermal fluids in simulation tools is critical for successful simulation studies. In this paper, we report the experimental and modelling work related to counter-current heat exchange and free drainage test runs in CIEMAT's multi-purpose MS test loop at Plataforma Solar de Almería in Spain. We present a general method to define MS and non-condensable gas within a homogeneous pressure-flow solver. We present modelling of an indirect MS TES system connected to a thermal oil loop through TEMA type heat exchangers, model calibration with half of the experimental data, and finally, validation simulations against rest of the data. All these experimental data are previously unpublished. The model predicts the system behaviour with good agreement regarding temperatures, pressures, flow rates and liquid levels. The simulations suggest that the heat exchangers' shell sides suffer from trapped non-condensable gas which significantly affects heat transfer, heat loss to ambient air and hydrodynamic losses. Our results contribute to thermal-hydraulic, system-wide modelling and simulation of MS processes. Furthermore, the results have practical implications for MS TES facilities with respect to system design, analysis and operation.

1. Introduction

Thermal energy storage (TES) can increase flexibility and efficiency for an application where thermal power generation is temporally misbalanced with the energy consumption or conversion. In Applied Energy, 165 TES papers were published between 2009 and 2017 [1], reflecting the importance of the topic. In concentrated solar power (CSP) plants, a TES system enables dispatchable electricity production during periods without sunlight (night hours, cloudy conditions). Additionally, TES can provide stability to the electricity network in case of high fraction of renewable production [2]. A properly sized TES decreases the specific cost of the solar field and may also increase the revenues from the electricity market, since the electricity price often rises after sunset hours [3]. Thereupon it is rational that majority of the

* Corresponding author.
E-mail address: jari.lappalainen@vtt.fi (J. Lappalainen).

https://doi.org/10.1016/j.apenergy.2018.10.009
Received 12 May 2018; Received in revised form 1 October 2018; Accepted 8 October 2018
Available online 16 October 2018

Nomenclature

Symbol	Description, Unit
A	cross-sectional flow area, m^2
c	polynomial coefficient for heat capacity, –
C_p	heat capacity, J/(kg K)
c_n	factor in Zukauskas formula, –
D	diameter, characteristic length, m
f	friction factor, –
h^*	specific enthalpy incl. flow kinetic energy, J/kg
h	specific enthalpy, J/kg
k	heat transfer tuning factor, –
l	polynomial coefficient for heat conductivity, –
$\dot{m}$	mass flow, kg/s
n	data point in the loss function calculation, –
Nu	Nusselt number, –
p	pressure, Pa
Pr	Prandtl number, –
Q	heat flux, W/m^2
r	radial co-ordinate; polynomial coefficient for density, m; –
Re	Reynolds number, –
s	tube arrangement dimension, m
S	source term for mass; momentum; energy, kg/(m·s); kg/s^2; $kg·m/s^3$
t	time, s
T	temperature, °C
v	fluid flow velocity, m/s
y	coefficient for dynamic viscosity, –
V	specific volume, m^3/kg
x	polynomial coefficient for compressibility; axial co-ordinate, –; m
z	spatial co-ordinate, m

Greek symbols

α	heat transfer coefficient, $W/(m^2 K)$
μ	dynamic viscosity, Pa·s
Δ	difference operator, –
λ	thermal conductivity, W/m
ρ	density, kg/m^3
χ	Isothermal compressibility, Pa^{-1}

Subscripts

avg	average
b	bulk
conv	convective
CST	cold salt storage tank
exp	experimental
HEX	heat exchanger
HST	hot salt storage tank
i, j	Indexes
in	Inlet
K	Kelvin temperature scale
loss	heat loss to environment
MS	molten salt
oil	thermal oil
out	outlet
s	shell side
sf	skin friction
sim	simulated
t	tube side
w	wall
0	Initial, reference

Abbreviations

AUTO	control loop automatic mode
CSP	concentrated solar power
CST	cold salt storage tank
DMS	direct molten salt
HEX	heat exchanger
HST	hot salt storage tank
HTF	heat transfer fluid
MAN	control loop manual mode
MOSA	Molten Salt Test Loop for Thermal Energy Systems at PSA-Ciemat
MS	molten salt
PSA	Plataforma Solar de Almería
SSE	sum of squared errors
TEMA	Tubular Exchanger Manufacturers Association
TES	thermal energy storage
UC	user component
1D	one-dimensional

recently installed CSP capacity has been integrated with TES [4].

Indirect two-tank molten salt (MS) storage system is the most widely used TES solution [4]. Commercial examples are the Andasol 1–3 plants in Granada, Spain, which couple solar fields using thermal oil as HTF to two-tank MS storage systems [5]. The other emerging option is direct molten salt (DMS) storage, which couples the storage system directly to a solar field. The DMS storage approach has also been proposed as a part of a hybrid solar-biomass combined cycle heat and power system [6]. Regarding the MS composition, molten nitrate salt mixtures are commonly used as heat transfer fluid (HTF) and storage media due to their preferred properties: high density and specific heat capacity, low chemical reactivity, vapour pressure, and cost [7]. However, the high melting point of 120–220 °C poses a challenge for the operation.

Modelling and simulation of CSP applications has been done at different levels of detail ranging from studies on a specific process component to plant-level control and operation. In this work, we applied system-wide dynamic process simulation (hereafter system simulation, for simplicity), which uses one-dimensional (1D) unit operation models. In contrast, computational fluid dynamics (CFD) models use significantly higher spatial resolution, which makes them computationally heavy, and therefore they are typically used to study phenomena within a single process unit, such as heat loss from a MS storage tank [2,8]. A variety of different modelling approaches for system simulation purposes exists, but altogether, the models typically provide a faster simulation speed than real time, and can be used for training, analysing and optimizing the plant operation and developing new control solutions. They are advantageous when the system performance in changing, realistic conditions is evaluated. Our modelling approach positions itself in a rigorous end of the system simulation, because we address both thermal phenomena and fluid dynamics.

Next, we give a brief review of the system simulation studies on CSP applications including TES. The control and operation strategy affects the performance and economics of the whole plant [9], which makes the topic one of the most studied among the system simulation publications. The dynamic simulation study of the commercial Andasol II parabolic trough plant in [10] indicated that the plant performance could be improved by testing operation strategies in a simulation environment with respect to the operator's decisions. Similar results are presented in [11], in which three different operation strategies in a DMS plant were compared using system simulation. Falchetta and Rossi [12] modelled and studied the operation of a 9 MW_e MS parabolic trough plant with two-tank indirect TES system, with a particular

emphasis on draining. Also Zaversky et al. [13] studied transient operational changes in an indirect two-tank MS TES system. Bonilla et al. [14,15] focused their dynamic modelling on the thermal oil–MS heat exchanger (HEX) system, the same one as we use in this study. Flueckiger et al. [16] studied long-term operation of a 100 MW_e power tower plant with a MS thermocline TES. Another model for MS thermocline TES was developed and validated against literature-derived theoretical and experimental data by Hernández et al. [17]. Vasallo et al. [18] used a system model for developing a model predictive control approach for optimal scheduling of a CSP plant with TES. Li et al. [19] presented a study of MS TES with charging and discharging simulations using rather simple, lumped parameter models. Li et al. [20] constructed a dynamic model of CSP system with a receiver and ceramic honeycomb TES, using air as HTF.

Recently, Rea et al. [21] introduced a novel CSP configuration with TES and a power block directly on a tower receiver and used system simulation for performance and techno-economic analysis. Cioccolanti et al. [22] conducted system simulation analysis to assist the forthcoming assembly and testing of a real prototype plant with a Fresnel reflectors solar field and an ORC unit coupled with a phase change material TES. Zhao et al. [23] developed and used CSP plant system simulation to improve the utilization of the packed-bed TES from the perspectives of a system-level operation and storage economy.

The dynamic process simulation software Apros, the platform used in this study, has also previously been used for studying CSP concepts. The different hybridization schemes of a direct steam generating linear Fresnel solar field and a conventional steam power plant were studied and compared in transient terms in [24,25]. A model for DMS two-tank storage system together with solar field using MS as HTF was developed in [26]. A dynamic model for commercial parabolic trough plant Andasol II was presented and validated by Al-Maliki et al. in [27] and further used for studying the plant operation and control during strongly cloudy periods in [10]. Study [28] examined a new concept combining a linear Fresnel solar field with supercritical CO_2 as HTF directly with a closed Brayton cycle, and in [29], this concept was compared to a concept combining a similar Brayton cycle to a MS solar field with a DMS two-tank storage system. These studies have, however, used the working fluid model without any quantitative assessment, which in contrast, is the main emphasis of the current study.

To computationally study the use of MSs as coolants, HTFs and storage media require reliable information on their thermodynamic properties. Basic information on the liquid phase of various molten salt mixtures is generally available, see e.g. [30,31]. However, descriptions of the fluid implementation in thermal-hydraulic codes with validation results are surprisingly rare considering the important role of MS in TES systems. Ferri et al. [32] implemented thermo-physical property functions for a MS mixture (60% $NaNO_3$ and 40% KNO_3) into the RELAP5 thermal hydraulic code. They presented a comparison based on experimental steady-state data with an electrical heater, including temperature and pressure information. They demonstrated the code performance with three transient simulations with a model of the Prova Colletori Solari (PCS) facility in Italy, but they did not present simulations against the measured transient data. Davis [33] presented an implementation of four different salt mixtures (Be, K, Li, Na, Zr fluorides) in the RELAP5-3D/ATHENA code for novel nuclear power applications, but did not present any simulation examples.

Flexibility and simplicity are important aspects for describing the working fluid in any simulation study, but especially in MS applications, where numerous MS mixtures are available, and new ones are under development [7]. The code should allow the user to define the fluid with the available limited property data. In this work, the fluid definition is based on simple property equations, which the user can parametrize. This is the first report, to the authors' knowledge, presenting a general fluid system for molten salts and applying it in a study aimed at calibrating and validating a TES system with respect to hydrodynamics and heat transfer.

This paper is organized as follows: Section 2 describes the test facility where we conducted the experimental part of the study. Section 3 presents the general context used in the computational part of the study, the new development for calculation of the working fluids, and the principles we used in the system modelling. The calibration and validation approach and the simulation results are presented in Section 4. Section 5 discusses and summarizes the main findings, while Section 6 briefly concludes the study.

2. Test facility description

In this study we used a MS test loop for thermal energy systems at Plataforma Solar de Almería (PSA) in Spain, referred to here as the MOSA facility, for producing data for model calibration and validation. The facility was designed by CIEMAT to study and evaluate materials and components, instrumentation and operation strategies with respect to using MS for TES [34]. An overall view of the facility is shown in Fig. 1, while Fig. 2 presents a simplified diagram of those parts relevant

Fig. 1. A view of the MOSA facility at PSA/Ciemat in southern Spain, showing the boiler (left, with chimney), hot salt tank with entering pipelines, a pair of heat exchangers, and insulated thermal oil and MS pipelines. The yellow safety rail on the far right indicates the pit of the cold salt tank. (For interpretation of the references to color in this figure legend, the reader is referred to the web version of this article.)

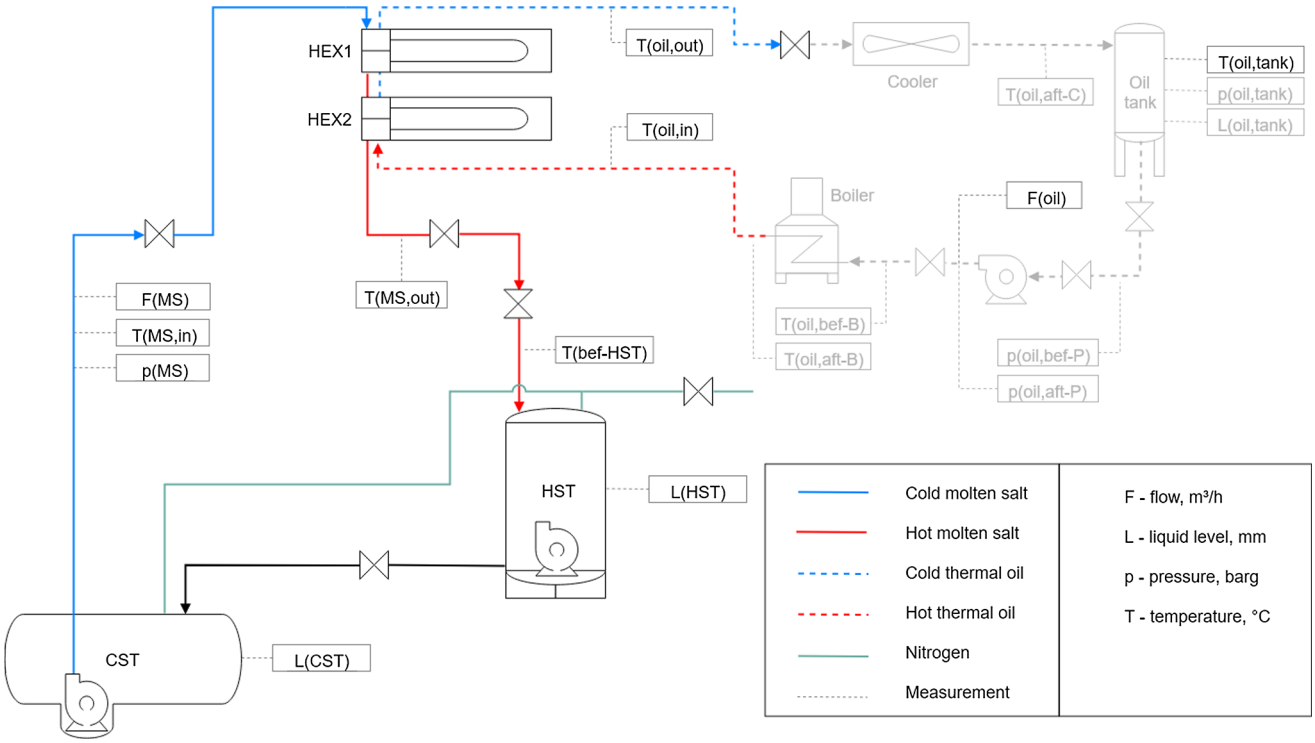

Fig. 2. Simplified process diagram of the MOSA parts used in this study. The colours indicate the cool (blue) and hot (red) sides of the system in a typical run in this study. The measurements in black were used in this study. (For interpretation of the references to color in this figure legend, the reader is referred to the web version of this article.)

in this study: cold salt tank (CST) and hot salt tank (HST) with centrifugal pumps inside, applied piping routes and valves for MS and thermal oil, two identical heat exchangers (HEX1, HEX2) in series, a gas line connecting the tanks, and instrumentation. The MS tanks and pipelines are mineral wool insulated. The tanks have electrical heaters and the pipelines are equipped with electrical heat tracing for prevention of MS freezing. The thermal oil loop exchanges heat with the MS side through the TEMA NFU type HEXs, and has capabilities for flow control by means of a centrifugal pump, and temperature control by means of a diesel boiler and air cooler. Solar salt (60% $NaNO_3$ and 40% KNO_3) is applied on the shell side, and Therminol VP-1 thermal oil on the tube side.

This paper focuses on a typical operating mode, where MS is pumped from CST to HST and heated/cooled by the oil loop using the HEXs in a counter-current configuration. Additionally, the periods when MS was drained from the HST to the CST via a connecting pipeline were analysed. The study thus investigates the most typical operations of a TES plant: charging, discharging and draining the system.

The MS storages are cylindrical insulated tanks: CST is horizontal and situated in a concrete pit below ground, HST is a vertical tank at ground level. The total salt mass in the system is approximately 40 metric tons. MOSA can be operated in a temperature range of 290–500 °C in general and particularly up to 380 °C when the MS–thermal oil HEXs are used. For details on the facility, see Refs. [34,14,15]. Fig. 2 presents the instrumentation used in this study. The terms 'in' and 'out' are used with respect to the HEX when the system is operated counter-currently. Primary measured quantities, related sensor types and measurement uncertainties are listed in Table 1. The MOSA control system was used for data collection with a sampling time of 5.0 s.

3. Methodology

3.1. Modelling and simulation environment

Apros is a commercial software platform [35] for system-wide modelling and dynamic simulation of process, automation and electrical systems. In this study, a new method to define a working fluid was implemented for the 1D homogeneous two-phase pressure-flow model [36], which is based on dynamic conservation equations for mass, momentum, energy and component masses. At each time step, in each calculation node, the thermodynamic state is solved from known enthalpy, composition and pressure to provide node temperature, gas volume fraction (or liquid level), phase composition, and fluid properties: density, dynamic viscosity, heat capacity, thermal conductivity, and density derivative with respect to pressure. See Appendix A for details of the thermal hydraulic solution. The following section describes the fluid property calculation developed and used in this study. A previous work for developing a new working fluid in the same environment is found in [37], targeted at seawater desalination

Table 1
Primary measured quantities, related sensors and uncertainties. Two values for thermocouples uncertainty are shown: the first is based on the sensor calibration practise, the latter is the general accuracy for a K type thermocouple.

Quantity	Type	Uncertainty
Temperature, MS/ thermal oil	K type thermocouple in thermowell	± 0.42/ ± 0.75%
Volumetric flow, thermal oil	Vortex type volumetric flow meter	± 0.75%
Volumetric flow, MS	Vortex type volumetric flow meter	± 1%
Pressure, MS	Resonant type gauge pressure transmitter	± 0.1% of the calibrated range (± 0.01 bar)
Liquid level, CST/ HST	Radar level transmitter	± 0.5 mm

applications.

3.2. Working fluid property calculation

In the case of MSs, there is a lack of information in the literature on the properties of the vapour phase. The vapour phase can, however, be neglected in typical solar power applications, because of the negligibly low vapour pressure at the working temperatures. For practical reasons, the systems use some non-condensable gas as a cover gas, which is consequently required in the modelling to allow simulation of storage tanks as well as start-up and shut-down procedures.

In the new fluid model, the user gives parameters for density, specific heat capacity, thermal conductivity, dynamic viscosity and compressibility as function of temperature by setting the parameters r_i, c_i, l_i, y_i and x_i in the equations below, where T is temperature, °C. Since density is considered as function of temperature and pressure, the equation below applies at the reference pressure. In the case of viscosity, an additive exponential term was provided to facilitate accurate definition.

$$\rho_0(T) = \rho(T, p_0) = \sum_{i=0}^{4} r_i T^i \tag{1}$$

$$C_p(T) = \sum_{i=0}^{2} c_i T^i \tag{2}$$

$$\lambda(T) = \sum_{i=0}^{4} l_i T^i \tag{3}$$

$$\mu(T) = \sum_{i=0}^{4} y_i T^i + y_5 \mathrm{e}^{\left(\frac{y_6}{y_7+T}\right)} \tag{4}$$

$$\chi(T) = \sum_{i=0}^{2} x_i T^i \tag{5}$$

The pressure-flow solution deals with compressible fluids, so we need to capture the pressure effect in the density calculation. The equation for density is deduced by starting from the definition of compressibility factor:

$$\chi = -\frac{1}{V}\left(\frac{\partial V}{\partial p}\right)_T \tag{6}$$

Considering density as the user-defined property (Eq. (1)), we obtain

$$\chi = \left(\frac{1}{\rho}\frac{\partial \rho}{\partial p}\right)_T \tag{7}$$

Taking integrals on both sides gives

$$\int_{p_0}^{p} \chi dp = \int_{\rho_0}^{\rho} \frac{1}{\rho} d\rho \tag{8}$$

wherefrom we can solve the density, and substitute the user-given density and compressibility equations to get:

$$\rho(T, p) = \rho_0(T)\mathrm{e}^{\chi(T)(p-p_0)} \tag{9}$$

Enthalpy can be expressed as follows:

$$h = h_0 + \int_{T_0}^{T} C_p dT + \int_{p_0}^{p} \left[V - T_K\left(\frac{\partial V}{\partial T}\right)_p\right] dp \tag{10}$$

where subscript 0 marks a reference state. Note that the multiplication with temperature T_K is in the Kelvin scale. Again, we use the user-given coefficients for density, leading to

$$h(T, p) = h_0 + \int_{T_0}^{T} C_p dT + \int_{p_0}^{p} \left[\frac{1}{\rho} + \frac{T_K}{\rho^2}\left(\frac{\partial \rho}{\partial T}\right)_p\right] dp \tag{11}$$

The derivative inside the brackets becomes

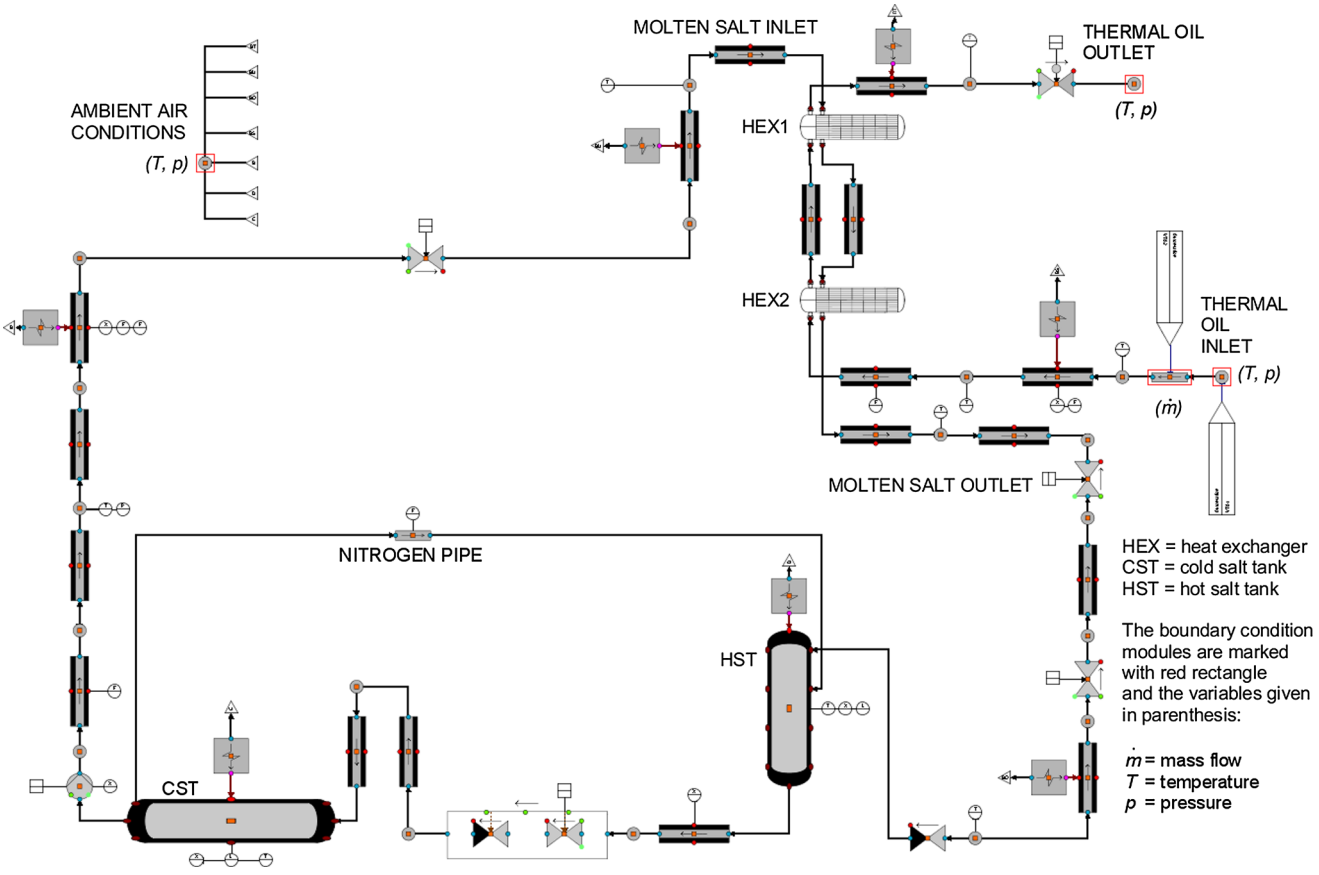

Fig. 3. Process model diagram including the parts of the facility relevant to the current study.

$$\left(\frac{\partial \rho}{\partial T}\right)_p = e^{\chi(T)(p-p_0)}\left[(p-p_0)\rho_0(T)\frac{d\chi(T)}{dT} + \frac{d\rho_0(T)}{dT}\right] \quad (12)$$

Now we get an equation for enthalpy, which includes the user-given polynomial functions, or their trivial derivatives and an integral:

$$h(T,p) = h_0 + \int_{T_0}^{T} C_p(T)dT + \frac{1-e^{(-p+p_0)\chi(T)}}{\chi(T)\rho_0(T)} + \frac{(T+273.15)}{\chi(T)^2\rho_0(T)^2}\left[\rho_0(T)\frac{d\chi(T)}{dT}) + \chi(T)\frac{d\rho_0(T)}{dT} - e^{(-p+p_0)\chi(T)}((1+(p-p_0)\chi(T))\rho_0(T)\frac{d\chi(T)}{dT} + \chi(T)\frac{d\rho_0(T)}{dT})\right] \quad (13)$$

Besides the MS fluid, which is assumed to have no vapour phase, the fluid system includes the cover gas. We used air in the implementation, although the target facility uses nitrogen for this purpose. Air is justified as a typical gas suitable for many different process systems. In the TES system the pressures are moderate, so air, being mainly composed of nitrogen, can be considered a good approximation of the cover gas. We used the simulation platform's existing calculation for air, based on tabulated data from [38,39]. The properties of the mixture of liquid and air are calculated according to the mixing rules. The mixture density is an inverse of the sum of the specific volumes of liquid and gas, the mixture specific heat is calculated as the mass-weighted arithmetic mean, and viscosity and thermal conductivity as the mass-weighted harmonic mean [40].

Table B1 in Appendix B shows the MS property functions that we used, as given by [41], except compressibility, which was calculated as the mass-weighted average of the $NaNO_3$ and KNO_3 values given in [42]. The Therminol VP-1 properties, shown in Table B2, were implemented according to the equations in [43], either directly or after minor refitting. In the reference, no value was given for compressibility; we selected a slightly higher value than water's, since oils are generally more compressible.

3.3. System modelling

Fig. 3 shows the graphical configuration of the process model, including only those parts of the MOSA facility that were relevant in the operational runs used in the current study. Control loops and measurements are not shown for brevity. The heat exchanger modelling is presented in Section 3.3.2.

For the model configuration we needed the equipment layout and elevations, heat exchanger materials and dimensions, CST and HST tank dimensions, piping material and dimensions (tube inside diameter and thickness, roughness, length of sections, loss coefficients), insulation material and thickness for heat exchangers, pipelines and tanks, pump curves, position of sensors, and control loops. This information was collected from the control display images, heat exchanger data sheet, and manufacturing documents, and also by tape-measuring and visual approximation at the facility. Most of this information can be found in

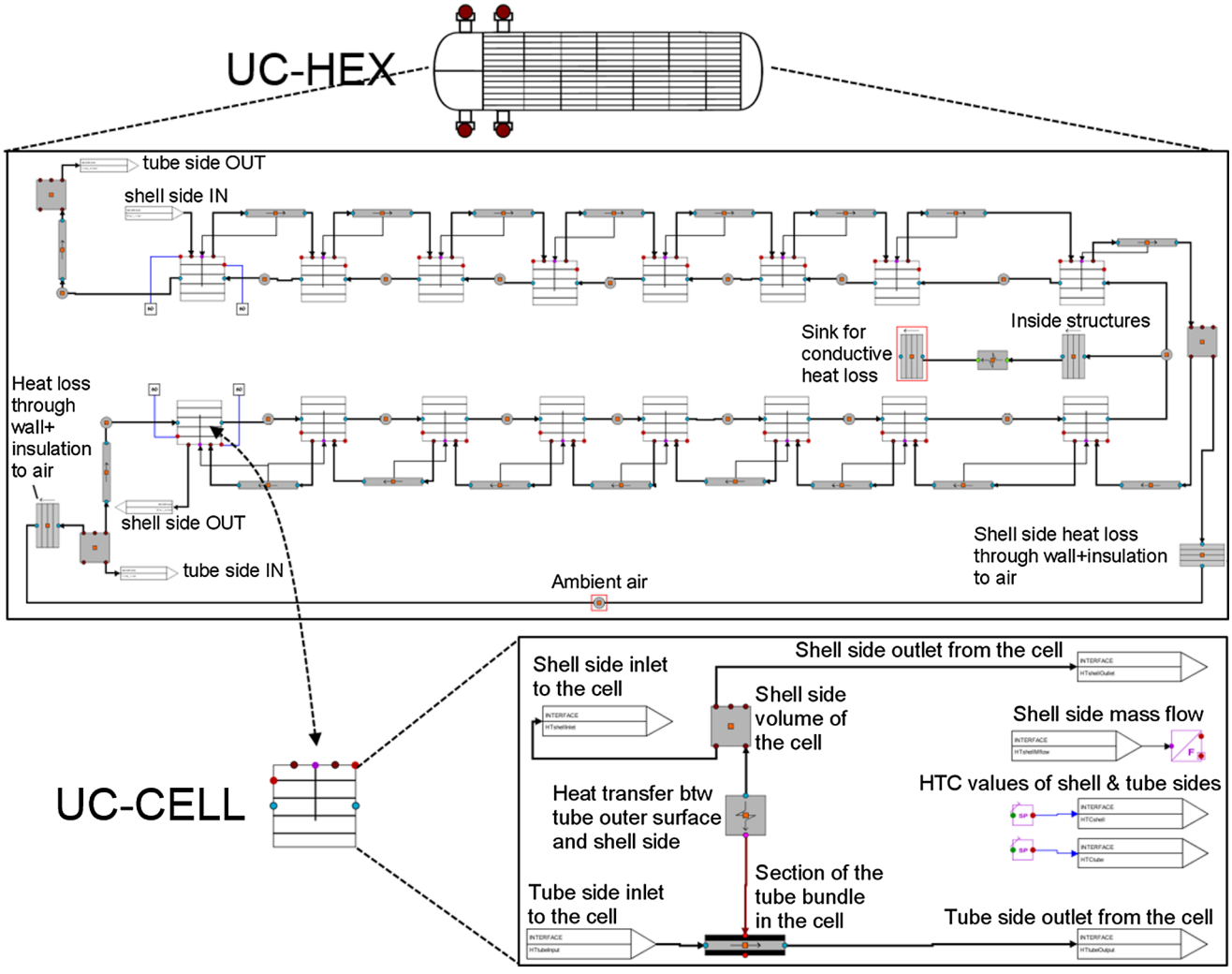

Fig. 4. Illustration of the HEX model structure applying two layers of User Components. The heat transfer correlations are defined in separate code scripts.

Refs. [15,34]. The material properties for carbon steel, stainless steel, and mineral wool were taken from literature and handbooks, see Appendix B.

3.3.1. Assumptions

While the aim of a dynamic simulation model is to predict the target process behaviour in a realistic way, calling for high fidelity in every aspect of the modelling, there are practical incentives to keep the model as simple as possible. Firstly, the effort required to build and parametrize the model should be reasonable. Secondly, the model should calculate the targeted simulations in reasonable time. The broader the scope of the simulation, the more emphasis is needed on maintaining a balance between details for accuracy and simplifications for speed and robustness. In this study, we used the following assumptions:

- Tanks are ideally mixed. In the facility, there are no mixers, but at the beginning of the test runs, the tank content was mixed by looping MS in a short circuit. This is common assumption in the system simulation studies. Modelling the temperature distribution and local heat losses, such as presented in [2], would dramatically slow down the calculation speed.
- Transportation of enthalpy and concentrations in the pipelines is based on sequential ideally mixed volumes. In this respect, also the nodalization scheme has an effect.
- The HEX structure is simplified with respect to the shell side baffle-separated volumes: 16 were used instead of 80 in the real system. The HEX modelling is described in Section 3.3.2.
- Constant ambient temperature (20 °C) and convective heat transfer coefficient (20 W/(m^2 K) were used in the convective heat loss calculation. Radiative heat losses were considered negligible and omitted.

Regarding nodalization of the pipelines, we used a maximum length of 1.0 m for those flow branches where dense discretization is relevant to better achieve the pipe delay. Shorter branches were used, too, when present in the real system, e.g. the valves. The model for a pipe section includes the carbon/stainless steel wall structures and the mineral wool insulation. The steel part is radially discretized into three layers, and the insulation is represented by a single layer. Heat loss from the outer surface to ambient air is calculated by convective heat transfer.

3.3.2. Heat exchanger modelling

The MOSA heat exchangers were pivotal equipment in our experiments. As mentioned previously, there are two identical HEXs in series where oil flows inside the tubes and MS in the shell side. Unfortunately, there is no temperature measurement between them. Instead of using the Apros standard HEX components, we designed and configured the units using the Apros User Component (UC) method in order to test effects of different nodalization schemes, heat transfer correlations, and heat loss configurations. The structure used in the study is presented in Fig. 4. The HEX component is composed of UCs at two levels, called here UC-HEX and UC-CELL. UC-HEX (Fig. 4, top) features (i) tube-side flow route, (ii) shell-side flow route, and (iii) thermal inertia and heat transfer to ambient air and mounting structures. The fluid routes are divided into 16 calculation volumes, which have been configured within the UC-CELL structure (Fig. 4, bottom) including a section of the tube bundle and shell volume, and heat transfer between them. In other words, the heat transfer mechanism is composed of convective heat transfer from oil to the tube wall, conduction through the wall, and convective heat transfer from the tube outer wall to the MS. In the case of cooling MS, the heat flow goes in the opposite direction.

The UC-CELL configuration includes the thermal mass of the tubes, according to the given dimensions and material. Additionally, thermal mass is introduced at the UC-HEX level as follows:

- Shell-side jacket, nozzles, head cover. Insulated, heat loss to ambient air.
- Tube-side end with inlet/outlet nozzles. Insulated, heat loss to ambient air.
- Inside structures: baffles, longitudinal baffle, separator plate between the sides. The baffles are tightly connected with the tubes' outer surface. We lumped together this mass for heat loss by conduction to HEX mounting/supporting structures (cold bridges). The boundary temperature for the sink metal in the model was set at 100 °C.

The steel mass of the HEX model totalled approx. 1300 kg, which is the documented mass given for one HEX unit.

The heat transfer correlations for the HEX tube and shell side are presented in the following. For the tube side, we tested the Dittus-Boelter, Sieder-Tate, and Gnielinski equations, and selected the latter because it covers a wide Re and Pr range.

$$Nu = \frac{(f/8)(Re_b - 1000)Pr_b}{1 + 12.7(f/8)^{1/2}(Pr_b^{2/3} - 1)}, \tag{14}$$

where the friction factor is

$$f = [0.79\ln(Re) - 1.64]^{-2} \tag{15}$$

The equation is valid for $2300 < Re_b < 10^4$ and $0.5 < Pr_b < 2000$.

For the shell side, where staggered tube bundles are in crossflow, we tested Dittus-Boelter, Donohue, Chilton-Colburn, and Zukauskas. We selected Zukauskas, thus using the following group of equations:

$$Nu = 1.04 c_n Re_b^{0.4} Pr_b^{0.36} \left(\frac{Pr_b}{Pr_w}\right)^{0.25} \quad 1 < Re_b < 500; \tag{16}$$

$$Nu = 0.71 c_n Re_b^{0.5} Pr_b^{0.36} \left(\frac{Pr_b}{Pr_w}\right)^{0.25} \quad 500 < Re_b < 10^3; \tag{17}$$

$$Nu = 0.35 c_n Re_b^{0.6} Pr_b^{0.36} \left(\frac{Pr_b}{Pr_w}\right)^{0.25} \left(\frac{s_1}{s_2}\right)^{0.2} \quad 10^3 < Re_b < 2{\cdot}10^5 \tag{18}$$

$$Nu = 0.031 c_n Re_b^{0.8} Pr_b^{0.4} \left(\frac{Pr_b}{Pr_w}\right)^{0.25} \left(\frac{s_1}{s_2}\right)^{0.2} \quad 2{\cdot}10^5 < Re_b < 2{\cdot}10^6 \tag{19}$$

Considering the *Re* range, the Eq. (18) is usually applied in this study. In Eqs. (18) and (19), the last term describes the arrangement of staggered tubes, and we approximated the ratio $\left(\frac{s_1}{s_2}\right)$ as 2.0 from the design information. There are more than 16 tube rows, so value 1.0 was used for the factor c_n.

The convective heat transfer coefficient is obtained from the Nusselt number by

$$\alpha = k_i Nu \frac{\lambda}{D} \tag{20}$$

where k_i is the heat transfer tuning factor, k_s for the shell side and k_t for the tube side. This factor is used in the model calibration.

The other convective heat transfer coefficients needed for the various wall surfaces are calculated as follows:

- For the metal surfaces which have heat loss through insulation to air, the Apros default correlation (Dittus-Boelter, see Eq. (A8)) was used for simplicity.
- A constant value of 20 W/(m^2 K) was used for the convective heat transfer coefficient from the insulation surface to ambient air.
- For the metal involved in the cold bridges, we introduced a convective heat transfer coefficient, which we used in the model calibration as a dominant parameter for the heat losses, as described in Section 4.1 below.

4. Simulation results

4.1. Approach

Before the experimental period in October 2017, we had prepared our first version of the MOSA facility model. We used the model for preparing plans for the coming experiments. After the experiments, we updated the model structure and parameters with the new information received: observations, practical operation experience, discussions with the plant personnel, and the measurement data. After these updates, our model had sufficient readiness to simulate the experimental tests. We continued with the following steps:

1. Define the scope and purpose of the present calibration and validation study.
2. Determine target quantities to compare the experimental and simulated results, and the primary model parameters affecting these quantities.
3. Divide the experimental data into two sets: calibration and validation.
4. Calibrate the selected model parameters to minimize discrepancy between simulation results and measurements with respect to the target quantities.
5. Run validation simulations according to the validation set, and finally, analyse the results.

Step 1. We defined the purpose of the model to adequately predict the system behaviour during operation with changes in MS and oil flow rates. In other words, the model had to be capable of capturing the characteristics and predict phenomena related to (i) heat transfer between the oil and MS, (ii) thermal inertia, i.e. the dominant heat capacities in the system, (iii) hydrodynamic losses in the system, and (iv) thermal losses.

The MOSA facility enables several different operating modes and MS routes. The main modes relate to charging and discharging of the TES system, but the route options and possibility to loop MS back to the tank increase the number of available different test runs. In this study, we focused on pumping MS from CST to HST while the oil loop heats the salt counter-currently. Altogether, eight such experimental periods were executed, all of which are included in this paper. One experiment with the same route, but performing cooling via the oil loop was conducted and included here. Occasionally, MS was drained from HST to CST to enable the next test. We used these periods as additional calibration and validation data with respect to the fluid friction forces. The experimental data sets are characterized in Table 2. The number in the test run name refers to a test day, and the letters a/b/c to a test section within a day, and Dr to the drainage period. The role of the test runs divides the data sets into calibration (Cal) and validation (Val) data.

We limited the model scope according to the target defined above. On the MS side, we included the countercurrent line from CST to HST via HEX, the gas line connecting the tanks, and the HST drainage line. In simulation studies it is generally desirable to operate the model as close to real operation as possible. Consequently, we replicated the use of the MS flow control loop. For the oil mass flow and oil temperature after the boiler, we used the measured values directly as the model boundaries. Furthermore, we used simulation command scripts to launch the same step changes as in the experiments. The conditions before each experimental test run varied considerably, but we decided to use an easy and consistent method for obtaining an initial state for the simulations. We prepared the initial state by simulating the conditions representing the start of the run period for 15 min.

Step 2. Because the MOSA facility has been targeted for general TES research purposes, it has fewer on-line measurements than research facilities especially targeted at thermal hydraulic code validation. Therefore, we could not conduct separate effect tests for friction, hydraulic losses or heat losses, instead the tests were integral in the nature. Fluid temperatures and pressures are the most interesting target quantities. We complemented this direct information with other, indirect measurements, to reach a better understanding of the system. Tank liquid level measurements are good examples of this; we used these to complement the flow measurements. Pump speeds provided valuable operational details. Our selected target quantities are shown in Table 3.

Heat loss from HEX, $Q_{HEX,loss}$, was estimated with the formula:

$$Q_{HEX,loss} = \dot{m}_{oil} \cdot C_{p,oil,avg}(T_{oil,in} - T_{oil,out}) - \dot{m}_{MS} \cdot C_{p,MS,avg}(T_{MS,out} - T_{MS,in}) \quad (21)$$

This is not temporally exact due to the system lags. Because heat losses are significant in this case, we selected it as one of the target quantities, but we used it only for such periods in the data that represent close to a steady state operation.

Step 3. We divided the CST-HST-counter data (9 runs) into two sets, calibration and validation, using simple rules. Firstly, we distributed the runs to both sets, considering both the number of data points, and the test day. Secondly, when there were two sets with approximately the same temperature range, they were separated. We also separated the two runs with fluctuating inlet oil temperature. Thirdly, we left our main experiment mimicking cloud cover (7a) for the validation set due to its wide temperature range. Also, the only run where MS was cooled was left to the validation set. The HST-drainage data (6 runs) was divided based on the initial MS level and temperature in HST: the run with the highest values, the one with the lowest values, and one with intermediate values were chosen for the calibration set. Altogether, we ended up with the division presented in Table 2.

Step 4. We planned the calibration simulations using full factorial experimental design. We defined the loss functions given in Table 4 to assess the goodness of the tuning parameters. As described previously, we selected the start and end times of each run so that we could include all sound data points that represent the selected operation mode. The data points included in the loss function calculation were not necessarily all points of the run. Due to the significant thermal inertia in the system, each CST-HST-counter run is influenced, for some time, by the conditions before the run. This period is not reasonable to include in the temperature loss functions, so we left out the first 10 min of the runs. This was not needed for the pressure or for the liquid levels, because thermal inertia does not play any role in those. With respect to heat

Table 2
Characteristics of the experimental runs used in this study.

Run	Start time	Operation	Duration	Role
1a	17.10.2017 10:58:00	CST-HST-counter, heating MS	3 h 22 min	Cal
1b	17.10.2017 15:21:00	CST-HST-counter, heating MS	33 min	Val
3a	19.10.2017 10:46:00	CST-HST-counter, heating MS	1 h 33 min	Val
5a	23.10.2017 11:04:45	CST-HST-counter, heating MS	3 h 10 min 45 s	Cal
5c	23.10.2017 14:38:30	CST-HST-counter, heating MS	59 min	Cal
6c	24.10.2017 15:24:45	CST-HST-counter, cooling MS	33 min	Val
7a	25.10.2017 11:11:00	CST-HST-counter, heating MS	2 h 7 min 5 s	Val
8b	26.10.2017 13:15:00	CST-HST-counter, heating MS	1 h 25 min 15 s	Cal
8d	26.10.2017 15:46:55	CST-HST-counter, heating MS	22 min 5 s	Val
1Dr	17.10.2017 14:45:40	HST-drainage	13 min 20 s	Cal
3Dr	19.10.2017 16:21:40	HST-drainage	9 min 20 s	Val
4Dr	20.10.2017 13:05:30	HST-drainage	43 min 20 s	Cal
5Dr	23.10.2017 14:16:10	HST-drainage	15 min 30 s	Val
6Dr	24.10.2017 16:03:15	HST-drainage	26 min 45 s	Cal
7Dr	25.10.2017 16:05:35	HST-drainage	24 min 50 s	Val

Table 3
Target quantities and related physical phenomena.

Target quantity	Heat transfer between oil and tube inside	Heat transfer between tube outside and MS	Heat losses	Hydro-dynamic losses
$T_{MS,out}$	X	X	X	
$T_{oil,out}$	X	X	X	
$Q_{HEX,loss}$	X	X	X	
P_{MS}				X
L_{CST}, L_{HST}				X

Table 4
Loss functions used in the model calibration (SSE = sum of squared errors).

SSE	Equation	Number
SSE_1	$\sum_{i=n0}^{n}\{(T_{MS,out,exp}(t_i)-T_{MS,out,sim}(t_i)\}^2$	22
SSE_2	$\sum_{i=n0}^{n}\{(T_{oil,out,exp}(t_i)-T_{oil,out,sim}(t_i)\}^2$	23
SSE_3	$\sum_{i=n1}^{n2}\{(Q_{loss,exp}(t_i)-Q_{loss,sim}(t_i)\}^2$	24
SSE_4	$\sum_{i=1}^{n2}\{(p_{MS,in,exp}(t_i)-p_{MS,in,sim}(t_i)\}^2$	25
SSE_5	$\sum_{i=1}^{n}[\{(L_{CST,exp}(t_i)-L_{CST,sim}(t_i)\}^2+\{(L_{HST,exp}(t_i)-L_{HST,sim}(t_i)\}^2]$	26

loss, we selected periods that were close to steady state. The liquid level loss function was used only in the drainage runs; it was applied to all data points.

We used the following tuning parameters in the calibration:

1. HEX tube side heat transfer efficiency
2. HEX shell side heat transfer efficiency
3. Convective heat transfer coefficient from the HEX oil side to metal connected with the cold bridge
4. HEX shell side pressure loss coefficient
5. Drainage piping pressure loss coefficient

Regarding the HEX parameters, we used equal values for both HEX units. The parameters 1–3 all affect the costs SSE_1, SSE_2 and SSE_3, so they were variated together by the full factorial design. These SSE values were calculated over the calibration runs (1a, 5a, 5b, 8b), and finally summed up to form a value representing total SSE. Parameter 3 (heat loss tuning) dominated the total SSE, and we were able to select a proper value for it. Then we repeated simulations with full factorial design for parameters 1 and 2, and achieved values for those too. It is worth mentioning that parameters 1 and 2 are strongly coupled. For example, reducing the tube-side efficiency and simultaneously increasing the shell-side efficiency results in comparable total SSE values. Parameter 4 was selected simply by summing up the SSE_4 values from the four calibration runs. In the drainage run calibration, we variated parameter 5 and summed up SSE_5 values over the three calibration runs (1Dr, 4Dr, 6Dr) and selected the value that provided the minimum total SSE.

Step 5. After the calibration, the model configuration and parameters were frozen, and simulations according to the validation test runs were executed. The calibration and validation results are presented in the next section.

4.2. Calibration results

The following figures present the calibration runs, measured (exp) values in red, and simulated (sim) results in blue. Fig. 5 presents the MS and oil mass flow rates. The flow sensors measure volumetric flow, which was converted into mass flow using the fluid temperature and the density formulas (Tables B1 and B2 in Appendix B). Since the MS fluid was our major interest, the changes were done predominantly on the MS side. The changes were executed stepwise, either by manual operation (MAN) of the flow control loop by means of the CST pump speed, or in automatic (AUTO) mode by changing the flow set point. The simulated and measured oil flow lines are congruent, because the measured signal was fed into the model as a mass flow boundary. Note that runs 1a and 5a are clearly longer than 5c and 8b.

Fig. 6 shows the MS tank liquid levels. As the runs are all from CST to HST, the levels evolve similarly. The good alignment between the measured and simulated levels shows that the model represents the tank volumes and dimensions accurately. As the levels are driven by the MS flow in the real system and in the model, this result also indicates that the MOSA level and flow measurements are in good agreement.

Fig. 7 presents the inlet and outlet temperatures of the thermal oil. The oil heats the MS in these runs. It was characteristic to the boiler that under certain conditions the temperature controller suffered fluctuations; this behaviour can be seen in runs 1a and 5a. The simulation follows the measured values rather well. The discrepancy in the early phase of the simulation is partly due to the fact that the model was oblivious of the operations before the start time. The simulation shows somewhat too fast responses, suggesting that the oil side modelling might lack some thermal inertia.

Fig. 8 presents the MS inlet and outlet temperatures. Generally, the simulation results follow the measured values. However, the 1a and 5a runs show a tendency that appeared in this study: the model overestimates the heat exchange to MS in low MS flows (see the flows in Fig. 5), and underestimates it in higher flows. Several heat transfer correlations were tested without success in this respect. The shell side heat transfer tuning factor could not remove this discrepancy. We

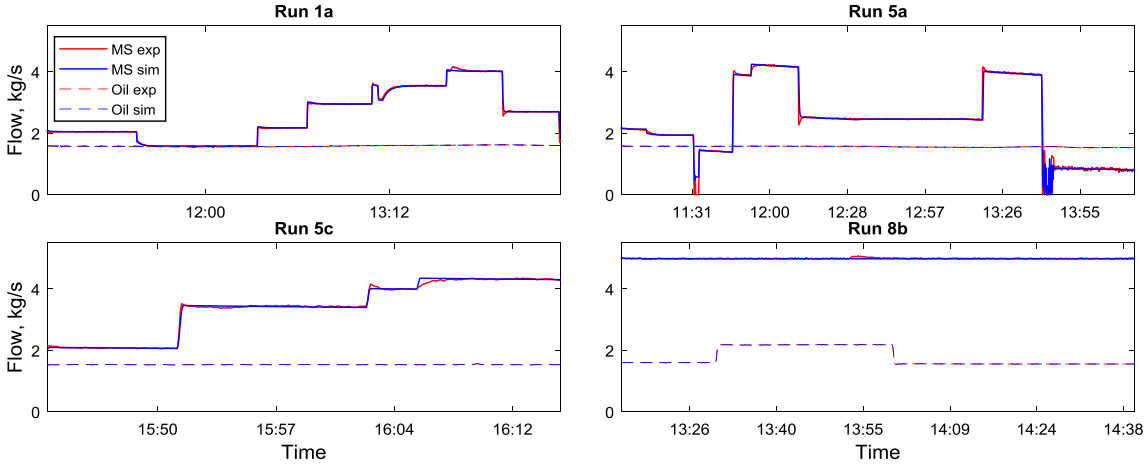

Fig. 5. Calibration results of the CST-HST-counter run: MS and thermal oil mass flows.

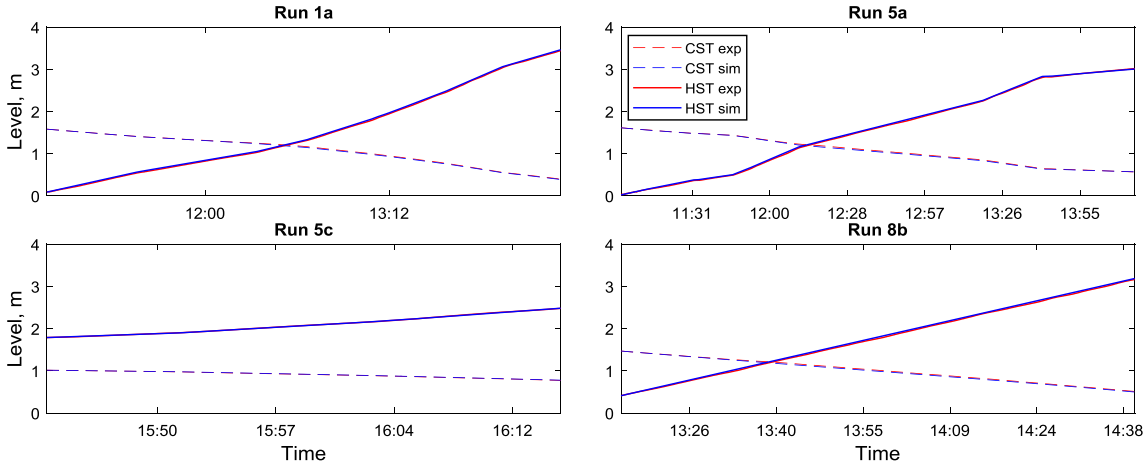

Fig. 6. Calibration results of CST-HST-counter run: CST and HST tank liquid levels.

noticed that this issue is also connected with the heat losses from the HEXs. Instead of extending our study to develop new correlations, we accepted this and used the Zukauskas and Gnielinski correlations, because their validity ranges (*Re*, *Pr*) cover the prevailing conditions. The large discrepancy in the initial periods of 1a and 5a are discussed further in the Discussion section.

Fig. 9 uses Eq. (21) to estimate the heat loss, i.e. it shows the difference between the heat flows that thermal oil delivers and MS receives. Thermal inertia in the HEXs and the dead times in the piping cause the anomaly of negative heat losses; this illustrates that this quantity gives a proper estimate only during steady states.

Fig. 10 shows all available information on the pressure on the MS side in this operation mode. The sensor is located before the HEXs, so it exposes the driving pressure needed to achieve the prevailing flow rate. No valves were throttled in these experiments.

The runs exhibit interesting events as indicated with the arrows in Fig. 10:

- 1a at 13:36: the experimental pressure suddenly drifts towards a new, lower level (from 2.01 to 1.88 bar g) without a set point change. Fig. 5 shows a simultaneous bump in the MS flow. The flow control is on AUTO, and thus corrects the flow rate back to the set point; to reach the same flow rate the pump needs 64.49% speed instead of 65.96% before the event (not shown in the figures). The model does not have any similar mechanism, so a clear discrepancy appears between the pressures (Fig. 10) and remains for the rest of the run.
- 8b at 13:53 repeats this anomalous behaviour: the pressure shifts to a new level and a simultaneous small bump occurs in the flow (Fig. 5).
- 5a at 11:53 and 5c at 16:06: the experimental pressure remains approximately constant, but the model prediction experiences a shift upwards. Fig. 5 reveals that the MS flow bumps up – in both runs. In both cases, the flow control loop is on MAN, so the pump speed stays at a constant value during the event. The simulation, in contrast, was run according to the measured flow rate, so we had this change included in the simulation script.
- The occurrence in 5a at 13:44 is also interesting. In the experiment, we manually set the pump speed to a low value, which collapsed the flow. This was soon noticed, and a higher speed was set, scarcely maintaining the flow. When comparing the pressure and flow levels, it seems that this occurrence returned the same level of hydrodynamic losses as at the beginning of the run.

It seems that a high enough MS flow suddenly decreases hydrodynamic losses in the MS flow path. It is noteworthy that the second high flow period in 5a did not repeat this pattern, probably because the lower pressure loss level did not return during the lower flow period. One interpretation of the phenomenon could be that gas is trapped inside a HEX and the gas bubbles resettle in the baffle-separated volumes in a way that reduces the hydrodynamic losses in the flow channel. Another explanation could be a release of a salt plug, although the return to the previous flow pattern goes against this interpretation. The response times from the flow increase to the pressure loss decrease in cases 1a, 5a, 5c and 8b are about 2, 7, 3 and 37 min, respectively. Thus, the timing is difficult to predict.

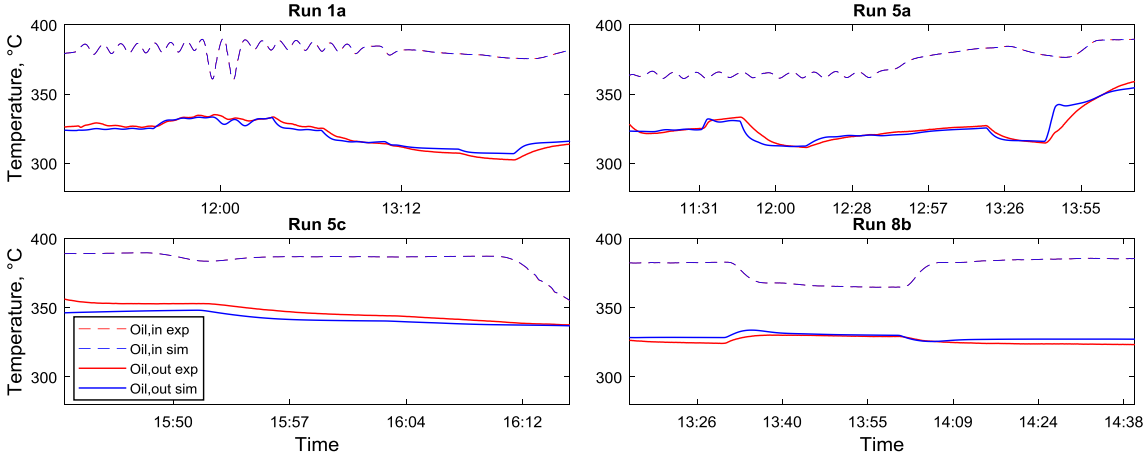

Fig. 7. Calibration results of the CST-HST-counter run: thermal oil temperatures.

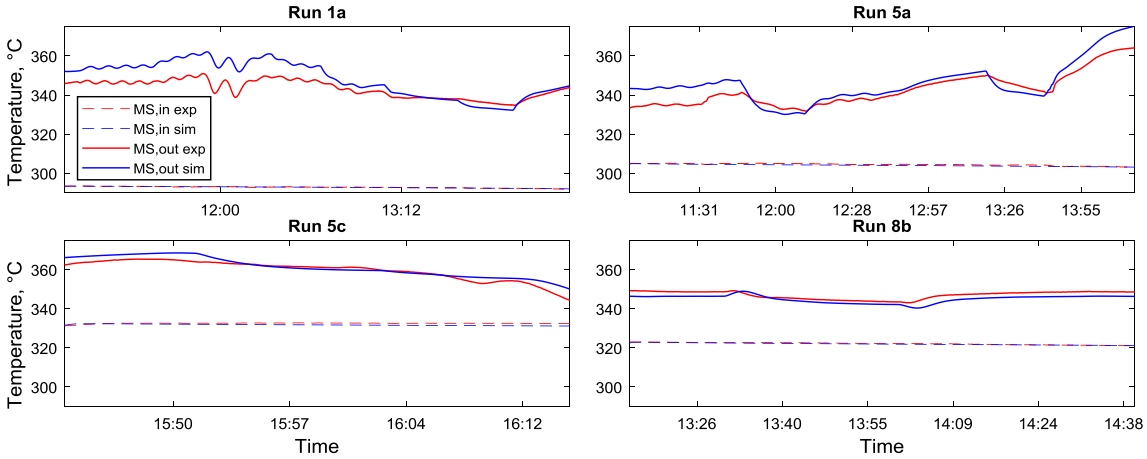

Fig. 8. Calibration results of the CST-HST-counter run: MS temperatures.

Fig. 11 shows the three calibration simulations for the HST drainage. The volumetric flows (top row) were calculated from the CST and HST liquid level measurements (bottom row). The level signals were moving averaged (3 points before and after) and then converted into volumes (m3), the gradients of which are presented here as estimated flow rates. The temperature of the drained MS was approximately 342, 330 and 318 °C in 1Dr, 4Dr and 6Dr, respectively. The results show that the optimized loss coefficient in the drainage pipeline is somewhat too large in case 1Dr, good in 4Dr, but too small in 6Dr.

4.3. Validation results

Here we present simulations with the calibrated model against the fresh measurements of the validation runs. The simulation experiments were conducted using the same initialization approach and boundary conditions. Fig. 12 shows the MS and oil mass flow rates in the runs. Again, as oil mass flow was used as a boundary, the measured and simulated values are on top of each other. Of the runs, 3a and 7a are the longest. Run 6c differs in that the oil side cools the MS. In 7a, we conducted so-called cloud cover experiments, i.e. caused a distinct reduction in heat production from the solar field, or in this case, from the boiler. For this reason, after an initial brief high flow period, the flow was reduced close to the nominal value and the control loop was set to MAN, thus maintaining a constant pump speed for the rest of the run. We can see the MS flow drifts downwards as expected due to the decreasing hydrostatic pressure in CST.

The tank liquid levels are shown in Fig. 13. There is good alignment between the measured and simulated levels.

Fig. 14 presents the MS inlet and outlet temperatures. The inlet remains almost constant due to thorough tank homogenization prior to each run, although a slight lowering takes place due to thermal losses. We can see that the model is capable of predicting the MS outlet temperature fairly well. Some observations:

- MS outlet temperature fluctuates in 1b, driven by substantial, regular fluctuation in oil inlet temperature, see Fig. 15. The simulation reproduces the behaviour, but with a smaller amplitude and a phase shift.
- The largest discrepancy in MS outlet temperature occurs in the first half of the short 1b run. Again, the beginning of the run is influenced by the different conditions prior the reference data. The overestimated heat transfer in this low flow (Fig. 12) period is aligned with the observation from the calibration runs. Run 3a further confirms that the heat transfer is overestimated in the low flow, which is best seen at 11:02.
- The model adequately reproduces the cooling run 6c. It is worth noting that the selected heat transfer correlations do not have any special treatment for cooling.
- 7a demonstrates how boiler shut-down drops the MS temperature two times in Fig. 14. Fig. 15 shows that the oil temperature decreases firstly by 69 °C and secondly by 93 °C. MS responds with dips of 38 and 49 °C in the measured, and 38 and 47 °C in the simulated data.

Fig. 15 presents the thermal oil inlet and outlet temperatures with respect to HEXs. Again, the inconsistency of the initial condition causes

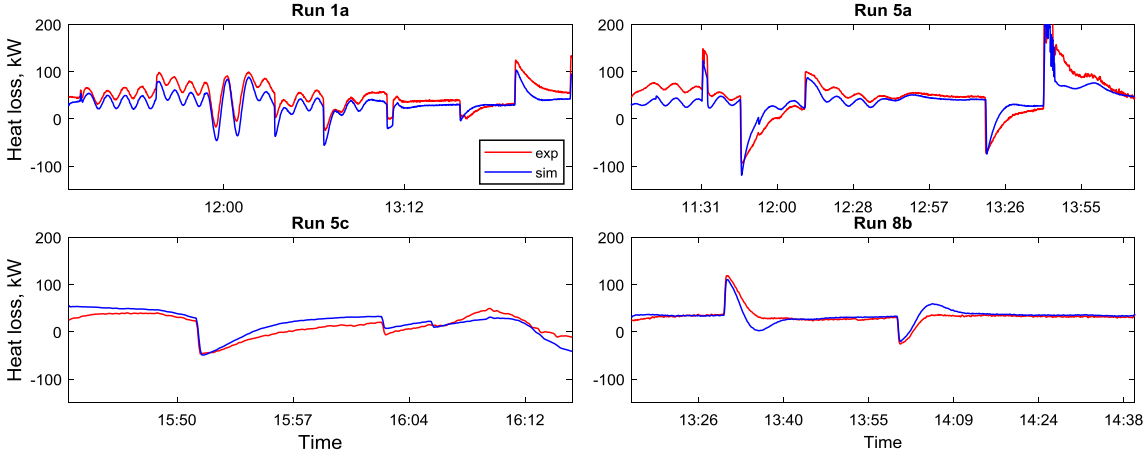

Fig. 9. Calibration results of the CST-HST-counter run: difference between heat flows from/to oil/MS (heat loss estimate).

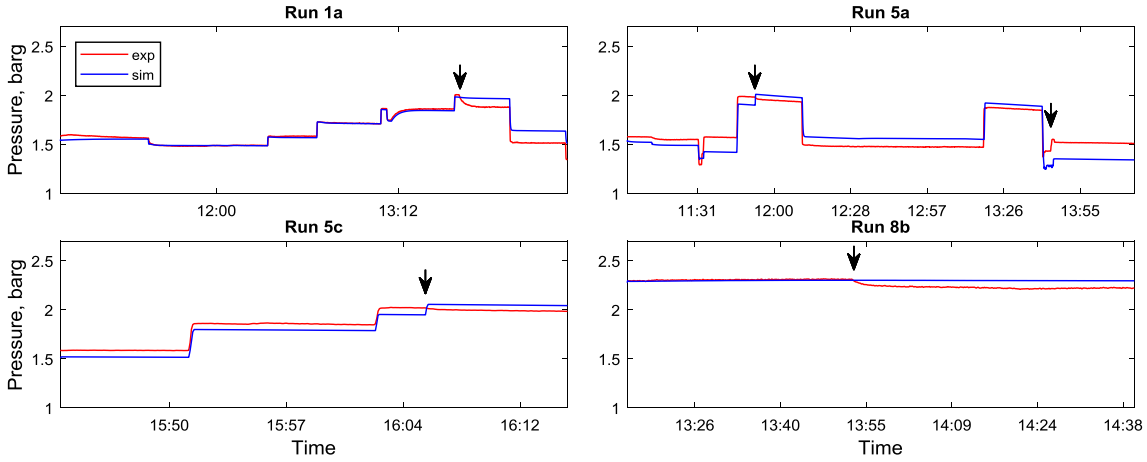

Fig. 10. Calibration results of the CST-HST-counter run: MS pressure before the HEXs. Arrows indicate sudden changes in hydrodynamic losses.

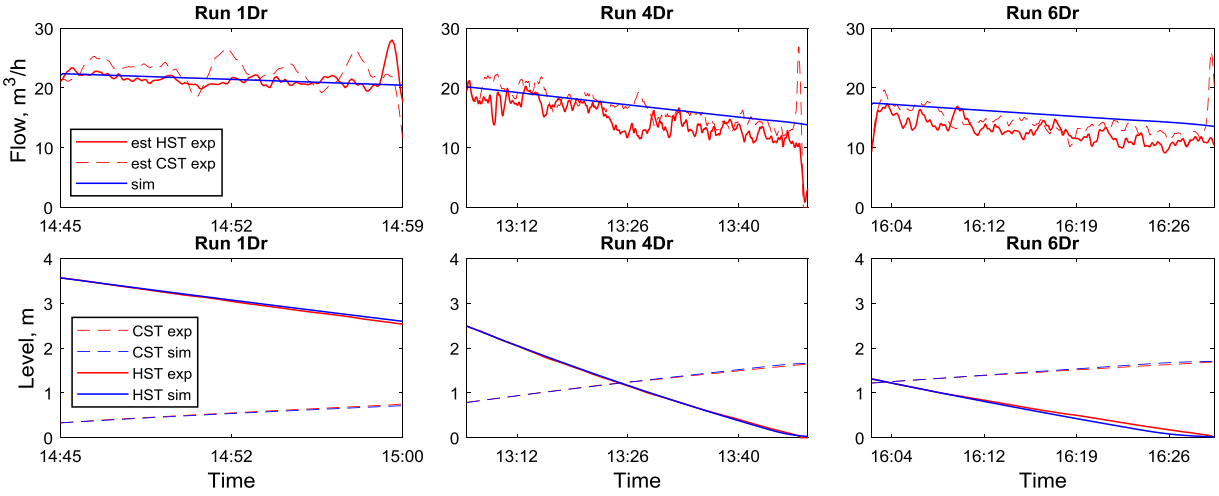

Fig. 11. Calibration results of the HST-drainage runs: estimated MS flows and tank liquid levels.

discrepancy (especially 1b, 3a and 7a) in the beginning of the runs. Run 6c differs due to the cooling mode. Run 7a reveals that the simulated oil side reacts faster than the experimental counterpart does. The calibration runs 1a and 5a already raised a suspicion of this.

Heat loss estimates according to Eq. (21) are shown in Fig. 16. Since the cooling run 6c used the same equation, now it is MS that delivers more heat than the oil side receives.

Fig. 17 reveals the pressure needed to move MS to HST. Again, no valve throttling was applied. The results are good in the sense that most changes are replicated with corresponding magnitude. It is interesting to reflect the previous observation of the sudden changes in hydrodynamic losses. Runs 6c and 8d feature this, i.e. constant pressure but

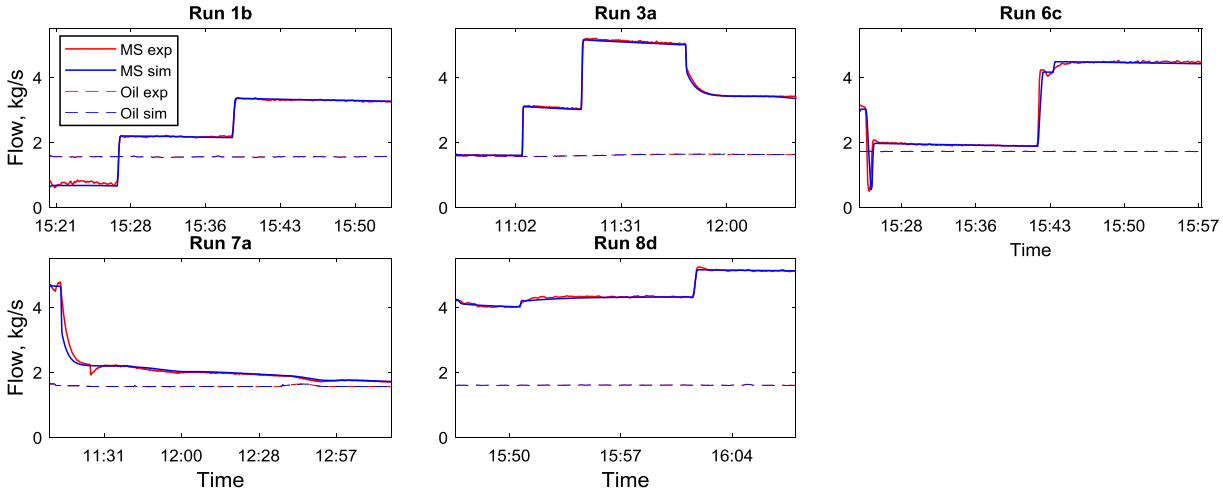

Fig. 12. Validation results of the CST-HST-counter run: MS and thermal oil flows.

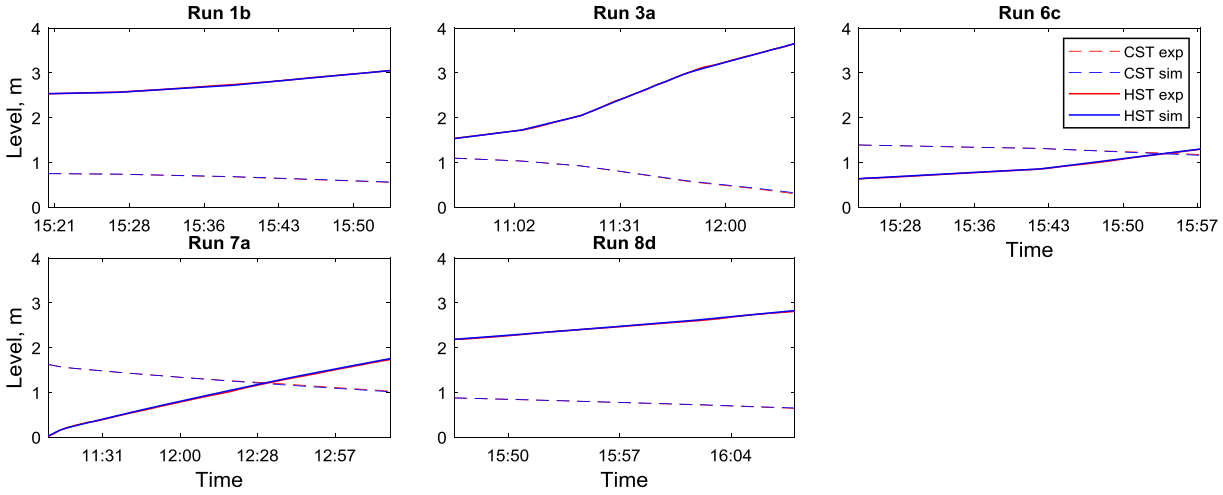

Fig. 13. Validation results of the CST-HST-counter run: CST and HST tank liquid levels.

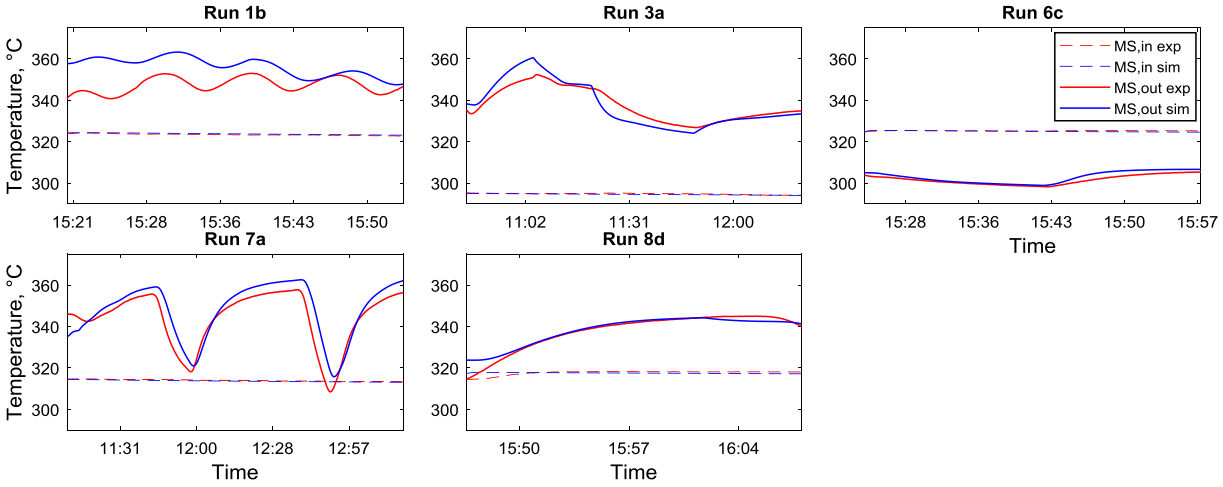

Fig. 14. Validation results of the CST-HST-counter run: MS temperatures.

increased flow, at 15:43 and 15:51 (Fig. 12), respectively. The flow control was on MAN, so we increased the CST pump speed in these spots to mimic this event in the simulations. Instead, run 3a reaches comparable MS flow rates (Fig. 12), but no abrupt effect can be seen. However, a sudden change does actually also take place there, simultaneously when moving to the highest flow (and pressure). We can infer this from the significantly changing flow-pressure ratio of the periods before and after the high flow part. In 7a, the flow is reduced in AUTO mode and it approaches the set point and then suddenly drops (Fig. 12), requiring the controller to increase the pump speed. As a consequence, a 0.16 bar higher pressure is required to reach the same flow.

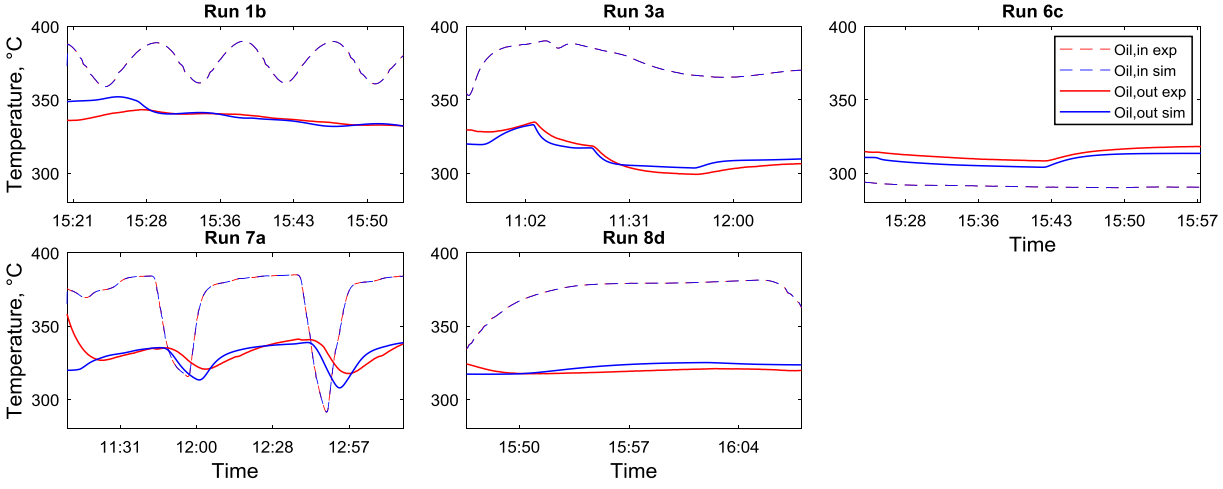

Fig. 15. Validation results of the CST-HST-counter run: thermal oil temperatures.

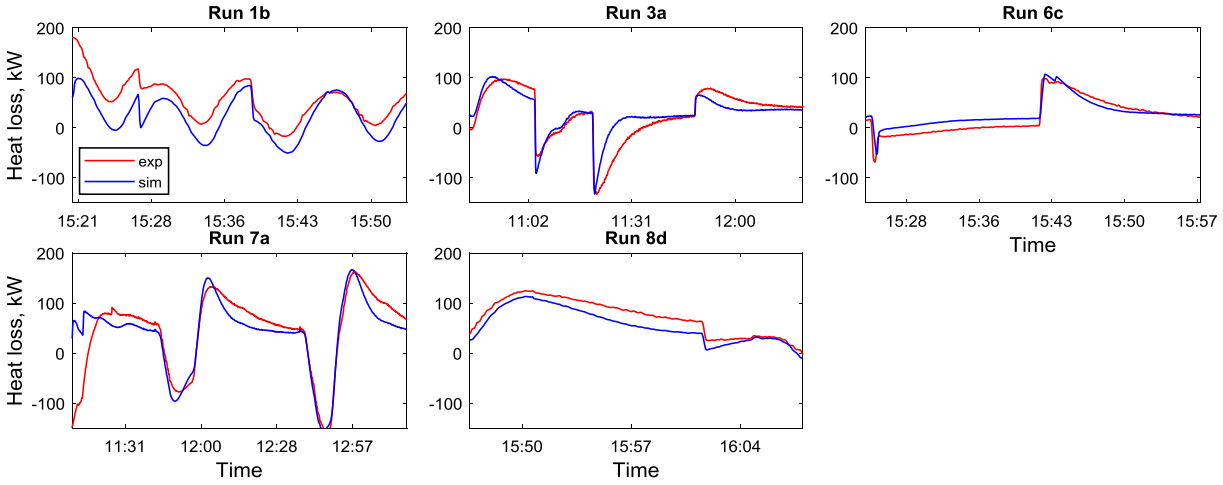

Fig. 16. Validation results of the CST-HST-counter run: difference between heat flows from/to oil/MS (heat loss estimate).

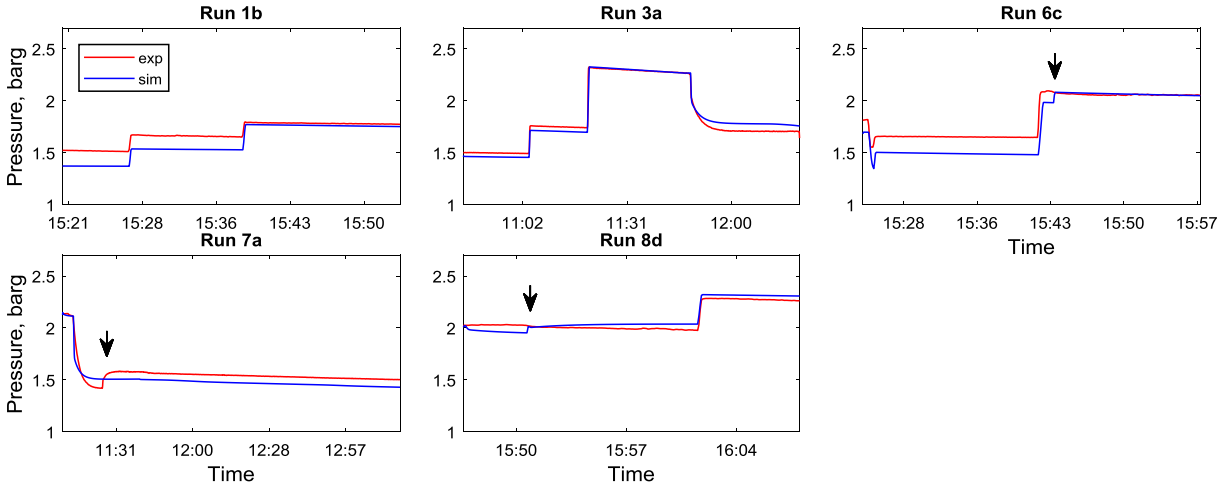

Fig. 17. Validation results of the CST-HST-counter run: MS pressure before HEX. Arrows indicate sudden changes in hydrodynamic losses.

Finally, Fig. 18 shows the validation simulations for the HST drainage runs. The average temperatures in these runs 3Dr, 5Dr and 7Dr were 323, 340 and 332 °C, respectively. The weakest prediction is for 5Dr, where the experimental drainage rate is higher than the simulated rate. Altogether, the results indicate that the fluid model and the homogeneous pressure-flow solver can predict the gravitationally driven flow reasonably well.

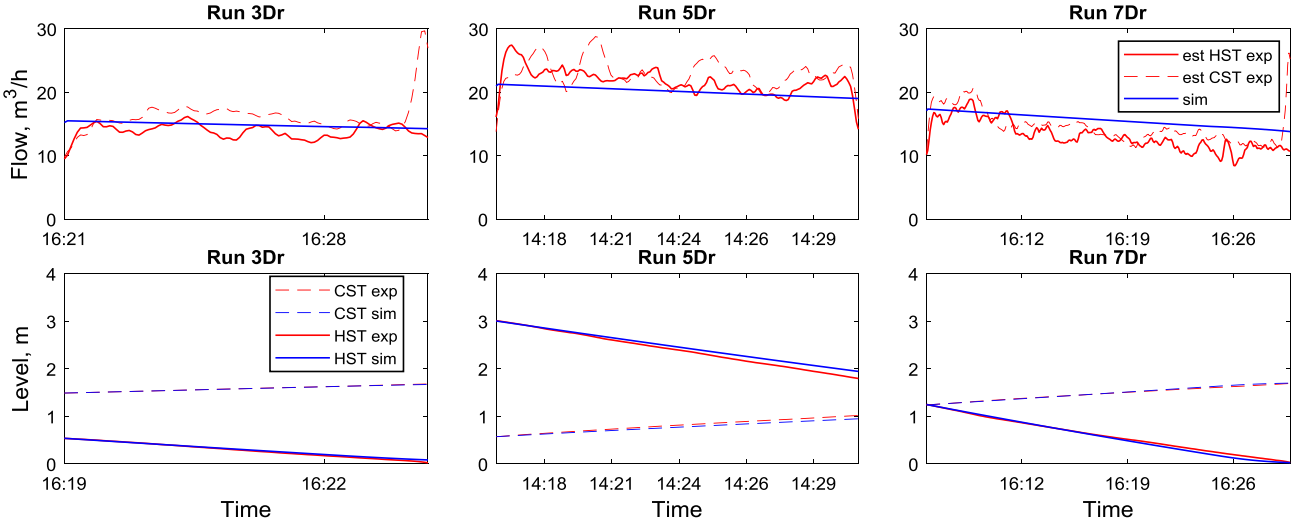

Fig. 18. Validation results of the drainage runs: estimated flows and tank liquid levels.

5. Discussion

We presented a method for incorporating a user-defined liquid and air within the 1D thermodynamic calculation, and applied the method in a dynamic TES system for describing molten salt (60% $NaNO_3$ and 40% KNO_3) and thermal oil (Therminol VP-1). The numerical method proved to work well in the test cases conducted. This method assumes that the liquid does not have vapour pressure; this is not an issue for MS with the typical temperature range used in CSP and TES systems. Therefore, we can generalize this method to be applicable across virtually all solar power applications.

Comparison of the experimental and simulation results did not indicate any need to modify the friction calculation in the homogeneous pressure-flow model used. In contrast, the heat exchanger modelling was more challenging. We constructed different HEX structures and tested them with various heat transfer correlations from the literature. The MOSA HEXs proved to have two special characteristics: a weakly performing shell side and occasionally surprisingly high heat losses to the environment.

Tables C1 and C2 list statistical metrics – mean error, mean absolute error and maximum absolute error – for numerical comparison of the experiments and simulations. Both calibration and validation runs are represented. The tank liquid levels are given for all runs, while the MS and oil temperatures as well as the MS pressure are relevant only to the CST-HST-counter runs. For temperature, the values were calculated by excluding the first 10 min of the data, since approximately this period is biased by the different history prior to the initial state in the experimental and computational experiments. The metrics are not given for the heat losses because the values are reasonable only for steady states, which were not consistently available. On average, the ratio between simulation time and real time was 17 with a standard laptop (2.6 GHz, 16 GB RAM).

Most of the runs are within the uncertainty with respect to the mean error and/or mean absolute error between the experimental and simulated temperatures, while the maximum deviation exceeds the measurement uncertainty (Table 1). We considered here the general relative accuracy for K type thermocouples, for example ± 2.25 and ± 3.00 °C in temperatures of 300 and 400 °C, respectively. In respect to tanks' liquid level, we noticed that the sensors cannot provide the given high accuracy in practise due to the demanding conditions of the installation and fluctuation in the liquid surface. We consider it as a very good result that the levels deviate only by a few millimetres in the best runs. The pressure results are good keeping in mind that the system featured a sudden change in hydrodynamic losses for which only speculative physical interpretations can be found. The MS and oil flow measurements were used as reference to conduct the simulation runs, in other words they were trusted as such. Regarding the comparison against measurement uncertainty, it is worth emphasizing that the uncertainty values given represent steady state conditions, and the metrics in Tables C1 and C2 were calculated from the transient conditions. Also, a small inaccuracy in timing of a step change in the simulation run can cause a large momentary deviation, causing a high value of maximum absolute error; this applies especially to rapidly responding quantities such as pressure.

The comparison metrics show similar results for both data sets, calibration and validation data. In the CST-HST-counter runs, the validation runs have even smaller deviations for the liquid levels. The other quantities show slightly higher error values in the validation set. This similarity in prediction capability is an encouraging result.

The modelling studies by Bonilla et al. [14,15] included two transient cases that are comparable to this study: (i) MS and oil flow rate changes, and (ii) cloud cover. We had several runs with flow rate changes, part of which reached comparable prediction accuracy with [14,15]. Their cloud cover experiment included one boiler stop, while we had two: a similar size and a larger one. They reported somewhat smaller maximum deviations than this study. However, it is worth noting the different approaches: they used the same data set to tune the model, while we tested with the fresh validation data, also including the case with 'clouds'. Our work also covers the larger scope of the MOSA facility. To summarize the comparison of this work with the earlier published simulations, we consider our model reached at least the same accuracy level than Bonilla et al. [14,15] with respect to thermal phenomena. Regarding the MS hydrodynamics, we did not find any comparable studies in the literature.

Our findings support the previously reported [14] finding that the shell-side results in poor performance of the HEXs. Our calibrated tuning factor for heat transfer was only 0.037 for the shell side, while 1.0 would correspond to the theoretical prediction by Zukauskas. Instead, for the tube side, our calibration resulted in a high heat transfer tuning factor of 2.0. The shell side dominates the overall heat transfer so strongly that the theoretical prediction (value 1.0) by Gnielinski could have been used with only minor changes in the results.

A plausible reason for the reduced heat exchange on the MS side is that the upper part of the shell side is not hydraulically full of MS, but has a substantial amount of cover gas. This was discussed in [34], emphasizing that the gas bubbles inside the HEX reduce the effective heat transfer surface, and that the drainage inclination and the baffles inherently trap some gas. We propose that in these runs, an even bigger contributor to gas trapping was the HEX filling from the top instead form the bottom when preparing for the counter-current runs. Practical reasons necessitated this unfavourable practise.

The applied heat transfer correlations, and the other ones tested, showed a tendency that the model overpredicts the heat transfer at low flow rate conditions, and underpredicts it at high flow rates. The literature correlations naturally assume the flow channel and heat transfer surface remains the same when the flow rate changes. In the case of gas inside the shell side, there are two reasons why the surface changes: the gas volume depends on the pressure, and the gas may resettle between the baffles due to changing hydrodynamic forces and MS liquid level. The former mechanism influences the observed direction, since a higher pressure decreases the gas volume and accordingly increases the MS volume, thus increasing the heat transfer surface. We found clear signs that also the latter mechanism is possible in the MOSA HEXs, as discussed below in the hydrodynamic loss paragraph.

Contrary to the findings of Bonilla et al. [14], our results show significant variation in the HEXs heat losses, perhaps because we studied a wider set of experimental data. The outside temperature and wind conditions were monitored during the tests: no clear correlation with heat loss was observed. Not all runs had clear steady state periods, but the results from the three selected runs give an implication of an inverse dependency between the HEX heat losses and the heat flow that MS receives, see Fig. 19. The open questions regarding heat losses lead us to propose that temperature sensors should be installed in the

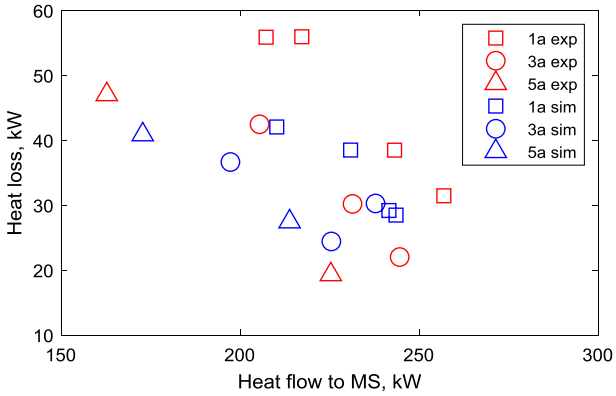

Fig. 19. Averaged heat loss estimates from three experimental and simulation runs. The averages represent periods where heat loss has practically reached a steady state.

support structures of TES facilities of this kind; this would give valuable information for the analysis and modelling of the heat losses. Also temperature sensors in the MS and oil pipes between the HEXs would be very beneficial for modelling studies like this.

Fig. 19 also shows the respective heat loss values for the simulations. The result reveals that the model substantially deviates from the experimental results in this respect and, additionally, it is less responsive to changes in the heat flow to MS. As described in Section 3.3.2 and 4.1 (Step 4), we tuned and fixed a parameter value for describing the heat transfer from the oil side to the HEXs walls and supporting structures, and then used it for all simulation runs. It seems that this simplification deteriorates the prediction capability, and is worthy of future development.

Our simulations showed a too rapid response from the oil inlet temperature to the oil outlet temperature, which was well aligned with the results of Bonilla and co-workers [14]. To overcome this issue, we tested several ways to divide the HEX model's thermal inertia between the oil and shell sides, while maintaining the actual total mass. Although we were able to improve the results, we did not achieve satisfactory alignment with the experimental temperature. After the calibration and validation study, we therefore conducted some additional simulation experiments to further investigate this aspect. Because run 7a shows best the discrepancy in response speed, we repeated it with additional thermal mass in the oil side pipelines. An increase in the tube wall thickness until approximately two tons of extra carbon steel accrued was needed to repeat the desired slowness with the model. However, this modelling solution is difficult to justify, and moreover, it affects the MS side making it overly slow. Another root cause for the slowness could be that the temperature measurement itself is excessively slow for some reason. This could be due to the T-branch located next to the sensor in MOSA. Again, we tested with 7a and found that similar slowness is reached if the temperature sensor's time constant is increased from our original 10–300 s.

Although not fully addressed in this paper, we also modelled the heat losses in the MS and oil pipes and MS tanks, leading to a minor downward drift in temperature. The share of the pipelines in the total heat exchange is minor compared to the HEXs. The simulated tank temperatures showed good agreement with the experimental ones. Large deviations were noticed only in the HST temperature during some drainage runs, probably due to the low mixing forces and the liquid level dropping below the sensors. We omitted the trends of these results for brevity.

We used the MS pressure after the CST tank in the CST-HST-counter run and the MS tanks' liquid levels in the HST drainage runs as reference in the calibration and validation of the hydrodynamic losses. The prevailing tank pressures are not measured, but the facility's experts assume the pressure always remains close to atmospheric. Some pressure variation might, however, take place, which causes a direct error source for our CST-HST-counter results. Namely, if the tanks' pressure level increases or decreases, it also influences the reading of the MS pressure sensor; there is currently no means of separating this phenomenon from possible real altering of the pressure loss in the MS line. This uncertainty could be reduced with new pressure sensors in the tanks.

The drainage results showed clear deviation in the drainage flow rates in half of the runs, seen as a growing difference between the simulated and experimental liquid levels. We could not fully identify reasons behind the discrepancy. Three aspects are worth mentioning. Firstly, it was noticed that during 1Dr, 4Dr and 5Dr there was additional activity around the CST: either CST homogenization or some MS returning to the CST from the earlier run. These both use a common, yet short pipe section with the HST drainage route. When reflecting this information against the drainage results, a minor pumping effect of the additional salt might be possible. Secondly, the role of MS temperature is worth further investigation as it affects the drainage rate and the HST temperature sensors showed altering temperature in some runs. Thirdly, the pressure balancing nitrogen line between the tanks has an important role: it maintains approximately equal pressures in the tanks, which influences operations where both CST and HST are used. Our simulations showed a maximum gas flow velocity of 1.5 m/s (CST-HST-counter) and 3.5 m/s (HST-drainage). The values are modest, so we conclude that the gas line is not a limiting factor for the MS flow. However, if additional routes for balancing the gas are open via the MS lines, the drainage flow could be affected; unfortunately we did not record this condition during the tests.

This work is the first modelling study using the pressure-flow approach in the modelling of the MOSA facility. In respect to pressure, the main rationalization behind the occasional deviation between the experimental and simulated values is that the model calibration compromised the two operational modes expressed by the hydrodynamic losses. The sudden, anomalous changes repeated when the operation moved from low MS flow rates to high, or vice versa. It is noteworthy that we noticed this couple of times during the actual MOSA experiments, but considered it as stochastic disturbances caused by solidified salt plugs in the connected pipelines (not shown in Fig. 3 for simplicity). According to the plant manager, the root cause for this behaviour was previously unknown. We managed to analyse it with a systematic method which can be applied in any similar process. This highlights the invaluable role of the first principles system model to analyse dynamic behaviour and uncover abnormal operation modes.

The MOSA facility was not designed for validating thermal hydraulic codes, which naturally limited the present study. However, our study shows that also a general research facility produces valuable information for such validation, especially when information from the primary sensors is complemented with other available measurements. The model proved to be a useful tool for understanding the mutual relationships of the system key quantities, assessing the reliability of existing measurements, and proposing advantageous new instrumentation for future studies.

6. Conclusions

In this study, we focused on two thermal energy storage system related cases: (i) pumping molten salt (MS) from cold tank to hot tank via a counter-current heat exchanger, and (ii) free drainage from the upper (hot) tank to the lower tank. We divided our experimental data into seven calibration and eight validation sets, and used the first set to tune the model and the latter set to test the model performance. Both sets are previously unpublished data. Using the presented working fluid calculation for the Apros pressure-flow solver, we built a system model and studied its capability to predict temperatures, pressures, flows and liquid levels in transient operations.

The dynamic system model showed good agreement when subjected to variations in MS and thermal oil flow rates and temperatures. It is notable that the prediction capability was similar among the calibration and validation data sets. We identified anomalous sudden changes in the hydrodynamic losses of the main MS flow route, and suggest that this is due to trapped gas inside the heat exchangers that resettles when the flow and/or pressure changes. The sudden change takes place to the direction of lower hydrodynamic losses when the flow rate (and pressure) reaches approximately 4 kg/s (and 2 bar g). The higher losses return after a hysteresis, when the flow and pressure come down to approximately 2 kg/s and 1.5 bar g. The phenomenon is stochastic in its timing.

In the test facility used, accurate predicting of the fluid temperatures after the heat exchanger was especially challenged by (i) reduced heat transfer on the shell side, (ii) heat losses to environment, and (iii) slow response of the thermal oil temperature after the heat exchanger. We suggest that the shell side's poor heat exchange (i), which also behaves against the commonly used correlations with respect to flow rates, and the variating heat losses (ii) are both connected with the cover gas that gets trapped inside the device in the filling phase. The

thermal oil efficiently exchanges heat to the tube walls and, apparently, the numerous baffles lead excess heat to the device walls and its supports if MS is not capable of sufficiently cooling the surfaces. We also discussed the oil-side slowness (iii) and proposed a slow sensor as a plausible explanation.

The findings we demonstrated, and similar that our method could potentially reveal, can significantly support engineers and plant owners in their discussions with equipment providers and system integrators. Malfunctioning process systems may have very large economic impact, which makes it important to pinpoint and prove the issues observed. The improved system understanding also benefits planning of experiments and system upgrades. Our results give a good basis for using the simulation code and the system model, or coming similar models, for studying the transient operation of thermal energy storage systems using MS. Besides the concentrated solar power applications, MS is used as a coolant in novel nuclear power concepts. Possible applications include system analysis, integrated process and control design, operator assistance and training. Online use as a tracking simulator could serve as a useful tool for fault diagnosis and performance assessment.

Acknowledgements

The authors gratefully acknowledge the funding for the experimental part provided by the EU 7th Framework Programme under the SFERA-II project, contract number 312643. The VTT authors also wish to acknowledge VTT Technical Research Centre of Finland for part funding this research, and address special thanks to the wonderful personnel at MOSA. Finally, the first author gratefully acknowledges the support from the Fortum Foundation, which significantly helped to finalize the work.

Appendix A

The Apros user configures the system model with component models that are conceptually analogous with the actual devices, such as pipes, valves, tanks, controllers, etc. These components can be configured to form new component models, so-called User Components. Accordingly, the system creates a network of thermohydraulic nodes, i.e. control volumes, and branches, i.e. connections between the nodes. This study used the Apros 1-D homogeneous two-phase model to solve the system pressures, enthalpies/temperatures, mass flows, mass fractions, and heat transfer between fluids and structures. The model can be written as partial differential equations with one axial co-ordinate z and time t as the independent variables. In a homogeneous two-phase model only conservation equations of the two-phase mixture are needed [36], as given by Eqs. (A1)–(A4), see Table A1. It is worth mentioning the specific enthalpy with flow kinetic energy is used. The S-terms on the right side of Eqs. (A1)–(A4) describe the sources of mass, momentum and energy. For the momentum equation, the source term may include pressure changes due to wall friction, pump, valves, and form loss coefficients. For the energy equation, it may include heat flows, energy dissipation due to friction, and pressure derivative in respect to time [36].

Table A1
Main equations of the homogeneous pressure-flow solution used in this study.

Description	Equation	No
Conservation of mass [36]	$\frac{\partial(A\rho)}{\partial t} + \frac{\partial(A\rho v)}{\partial z} = S_j$	A 1
Conservation of mass fractions	$\frac{\partial(A\rho x_i)}{\partial t} + \frac{\partial(A\rho v x_i)}{\partial z} = S_j$	A 2
Conservation of momentum [36]	$\frac{\partial(A\rho v)}{\partial t} + \frac{\partial(A\rho v^2)}{\partial z} + \frac{\partial(Ap)}{\partial z} = S_j$	A 3
Conservation of energy [36]	$\frac{\partial(A\rho h^*)}{\partial t} + \frac{\partial(A\rho v h^*)}{\partial z} = S_j$	A 4
Pressure loss due to friction or form losses	$\Delta p = -\frac{1}{2}\frac{k_{sf}\ \rho\ \lvert v\rvert\ v}{D_H}$	A 5
Heat conduction	$\rho C_{p,w}\frac{\partial T}{\partial t} = \frac{1}{r}\frac{\partial}{\partial r}\left[r\lambda\frac{\partial T}{\partial r}\right] + \dot{q}$	A 6
Convective heat transfer	$Q_c = \alpha_{conv} A (T - T_w)$	A 7
Heat transfer coefficient for one-phase forced convection (Dittus-Boelter)	$\alpha_{conv} = 0.023\frac{\lambda}{D} Re^{0.8}\ Pr^{0.4}$	A 8

The dynamic balance equations are discretized with respect to the spatial co-ordinate using a staggered grid approach: the mass and energy solution deals with the centre points of the mesh (nodes), and the momentum solution uses the intermediate positions (branches) between the mesh centres. The non-linear terms are linearized for the solution. The time integration method is backward Euler. The simulation time step is automatically decreased in case of large process transients to achieve convergence and to maintain accuracy in results. In the simulation, the mixture of substances moves along the process paths, driven by the pressure difference. Depending on the pressure conditions, the flow direction can also change. In the phase separated nodes, such as tanks, the quality of the outlet flow depends on the liquid level in respect to the elevation of the outlet stream connection [36].

The pressure loss due to friction or form losses in the piping network is calculated with Eq. (A5). The skin friction factor is calculated based on the surface roughness and current flow conditions, using the same approach as in [44].

The user defines construction materials (such as carbon steel) for the model components, where it is generally required (such as heat exchangers), or required due to targeted high accuracy (basic equipment such as pipes, tanks, valves, etc.). The heat structures introduce the dynamic features coming by means of thermal mass and heat conduction. 1-D heat conduction in a radial direction (e.g. through pipe wall) is calculated as given in Eq. (A6). Heat flow between fluid and the equipment wall is calculated with Eq. (A7). By default, the heat transfer coefficient of one-phase forced convection is calculated with the Dittus-Boelter correlation (A8). This study used other correlations as was described in the main text.

Appendix B

See Tables B1–B3 for the properties of the fluids and materials.

Table B1
Thermodynamic and transport properties of the MS.

Variables	Description	Constant/Correlation	Unit
T_o	Solidification temperature [41]	221	°C
h_o	Reference enthalpy	161,000	J/kg
r_i (i = 0, 1)	Density	$\rho = 2090 - 0.636 \cdot T$	kg/m^3
c_i (i = 0, 1)	Specific heat capacity [41]	$c_p = 1443 + 0.172 \cdot T$	J/(kg°C)
l_i (i = 0, 1)	Thermal conductivity [41]	$k = 0.443 + 1.9 \cdot 10^{-4} \cdot T$	W/(m°C)
y_i (i = 0–3)	Dynamic viscosity [41]	$\mu = 22.714 - 0.120 \cdot 10^{-3} \cdot T + 2.281 \cdot 10^{-7} \cdot T^2 - 1.474 \cdot 10^{-10} \cdot T^3$	Pa s
x_i	Compressibility	$2.124 \cdot 10^{-10}$	Pa^{-1}

Table B2
Thermodynamic and transport properties of the thermal oil Therminol VP-1 [43].

Variables	Description	Constant/Correlation	Unit
T_o	Solidification temperature	12	°C
h_o	Reference enthalpy	0	J/kg
r_i (i = 0–2)	Density	$\rho = 1083.25 - 0.90797 \cdot T + 7.8116 \cdot 10^{-4} \cdot T^2 - 2.367 \cdot 10^{-6} \cdot T^3$	kg/m^3
c_i (i = 0, 1)	Specific heat capacity	$c_p = 1492 + 2.846 \cdot T - 3.238 \cdot 10^{-4} \cdot T^2$	J/(kg°C)
l_i (i = 0, 1)	Thermal conductivity	$k = 0.137743 + -8.19477 \cdot 10^{-5} \cdot T - 1.92257 \cdot 10^{-7} \cdot T^2 + 2.5034 \cdot 10^{-11} \cdot T^3 - 7.2974 \cdot 10^{-15} \cdot T^4$	W/(m°C)
y_i (i = 6–8)	Dynamic viscosity	$\mu = 3.781 \cdot 10^{-5} \cdot e^{\left(\frac{821.1}{153.3+T}\right)}$	Pa s
x_i	Compressibility	$6.0 \cdot 10^{-10}$	Pa^{-1}

Table B3
Material properties of the equipment walls and insulation were considered constant or described as polynomial functions of temperature (T, °C).

Material	Density, kg/m^3	Heat capacity, J/(m^3 °C)	Thermal conductivity, W/(m°C)
Mineral wool	80	67,200	$0.062 + 0.000102 \cdot T$
Stainless steel	7800	$3811000 + 1233 \cdot T - 0.08591 \cdot T^2$	$12.74 + 0.0189 \cdot T$
Carbon steel	7800	$3315000 + 6029.4 \cdot T - 13.182 \cdot T^2 + 0.017316 \cdot T^3$	$54 - 0.0333 \cdot T$

Appendix C

Tables C1 and C2 present statistics on the error between experimental and simulated quantities. Each table presents one or two target quantities. All relevant calibration runs are listed first, followed by the relevant validation runs. The metrics are:

- ME = average error
- MAE = mean absolute error
- maxAE = maximum absolute error

Table C1
Statistical comparison between experiments and simulations: CST and HST liquid level.

		L_{CST}			L_{HST}		
Run	Role	ME	MAE	maxAE	ME	MAE	maxAE
1a	cal	9.5	9.5	22.2	−20.3	20.4	33.0
5a	cal	12.2	12.3	29.6	−15.1	16.4	36.4
5c	cal	−2.7	2.7	5.4	0.7	2.8	9.0
8b	cal	16.1	16.1	26.9	−23.0	−23.0	38.9
1Dr	cal	15.4	15.4	34.7	−27.7	28.2	62.2
4Dr	cal	−9.7	13.3	38.0	−0.5	14.0	40.0
6Dr	cal	−18.3	18.4	43.7	46.0	46.1	99.5
1b	val	−5.1	5.1	8.7	4.4	4.6	16.5
3a	val	−6.4	7.3	23.2	0.4	5.3	22.3
6c	val	3.7	4.8	18.9	−6.3	6.3	16.6
7a	val	7.8	8.6	21.3	−14.0	15.1	27.6
8d	val	−3.7	3.7	8.7	8.4	8.8	18.7
3Dr	val	1.9	2.2	10.8	−14.4	15.9	60.8
5Dr	val	38.9	38.9	68.8	−66.6	67.5	148.2
7Dr	val	−7.0	10.4	30.8	21.9	29.6	69.8

Table C2
Statistical comparison between experiments and simulations: MS and thermal oil temperature, and MS pressure. Quantities are relevant only in the CST-HST-counter runs.

		T_{MS}			T_{oil}			p_{MS}		
Run	Role	ME	MAE	maxAE	ME	MAE	maxAE	ME	MAE	maxAE
1a	cal	−5.1	5.7	16.5	−0.2	2.3	6.9	0.014	0.032	0.201
5a	cal	−3.0	4.3	11.0	0.1	2.5	18.9	0.012	0.092	0.384
5c	cal	−0.6	1.4	5.7	3.7	3.7	6.2	0.032	0.063	0.123
8b	cal	1.9	2.0	4.2	−2.4	2.4	4.8	−0.035	0.043	0.089
1b	val	−6.8	6.8	14.9	0.7	1.1	2.7	0.083	0.083	0.164
3a	val	0.6	3.2	9.6	−1.4	3.6	6.3	−0.006	0.037	0.248
6c	val	−1.5	1.5	2.9	3.9	3.9	4.7	0.088	0.093	0.413
7a	val	−4.5	5.1	17.4	0.7	3.8	13.2	0.059	0.067	0.240
8d	val	0.6	1.1	2.5	−4.1	4.1	4.8	−0.017	0.041	0.083

References

[1] Yan J, Yang X. Thermal energy storage. Appl Energy 2018. https://doi.org/10.1016/J.APENERGY.2018.03.001.
[2] Rodríguez I, Pérez-Segarra CD, Lehmkuhl O, Oliva A. Modular object-oriented methodology for the resolution of molten salt storage tanks for CSP plants. Appl Energy 2013;109:402–14. https://doi.org/10.1016/j.apenergy.2012.11.008.
[3] González-Portillo LF, Muñoz-Antón J, Martínez-Val JM. An analytical optimization of thermal energy storage for electricity cost reduction in solar thermal electric plants. Appl Energy 2017;185:531–46. https://doi.org/10.1016/J.APENERGY.2016.10.134.
[4] Peiró G, Gasia J, Miró L, Prieto C, Cabeza LF. Experimental analysis of charging and discharging processes, with parallel and counter flow arrangements, in a molten salts high temperature pilot plant scale setup. Appl Energy 2016;178:394–403. https://doi.org/10.1016/J.APENERGY.2016.06.032.
[5] Dinter F, Gonzalez DM. Operability, reliability and economic benefits of CSP with thermal energy storage: first year of operation of ANDASOL 3. Energy Procedia 2013;49:2472–81. https://doi.org/10.1016/j.egypro.2014.03.262.
[6] Pantaleo AM, Camporeale SM, Miliozzi A, Russo V, Shah N, Markides CN. Novel hybrid CSP-biomass CHP for flexible generation: thermo-economic analysis and profitability assessment. Appl Energy 2017;204:994–1006. https://doi.org/10.1016/j.apenergy.2017.05.019.
[7] Vignarooban K, Xu X, Arvay A, Hsu K, Kannan AM. Heat transfer fluids for concentrating solar power systems – A review. Appl Energy 2015:146. https://doi.org/10.1016/j.apenergy.2015.01.125.
[8] Suárez C, Iranzo A, Pino FJ, Guerra J. Transient analysis of the cooling process of molten salt thermal storage tanks due to standby heat loss. Appl Energy 2015;142:56–65. https://doi.org/10.1016/j.apenergy.2014.12.082.
[9] Roca L, Bonilla J, Rodriguez-Garcia MM, Palenzuela P, De La Calle A, Valenzuela L. Control strategies in a thermal oil – Molten salt heat exchanger. AIP Conf Proc 2016:1734. https://doi.org/10.1063/1.4949227.
[10] Al-Maliki WAK, Alobaid F, Starkloff R, Kez V, Epple B. Investigation on the dynamic behaviour of a parabolic trough power plant during strongly cloudy days. Appl Therm Eng 2016;99:114–32. https://doi.org/10.1016/j.applthermaleng.2015.11.104.
[11] Wagner PH, Wittmann M. Influence of different operation strategies on transient solar thermal power plant simulation models with molten salt as heat transfer fluid. Energy Procedia 2013;49:1652–63. https://doi.org/10.1016/j.egypro.2014.03.174.
[12] Falchetta M, Rossi AG. Dynamic simulation of the operation of a molten salt parabolic trough plant, comprising draining procedures. Energy Procedia 2013;49:1328–39. https://doi.org/10.1016/j.egypro.2014.03.142.
[13] Zaversky F, Rodríguez-García MM, García-Barberena J, Sánchez M, Astrain D. Transient behavior of an active indirect two-tank thermal energy storage system during changes in operating mode – An application of an experimentally validated numerical model. Energy Procedia 2014;49:1078–87. https://doi.org/10.1016/j.egypro.2014.03.117.
[14] Bonilla J, De La Calle A, Rodríguez-García MM, Roca L, Valenzuela L. Experimental calibration of heat transfer and thermal losses in a shell-and-tube heat exchanger. In: Proc. 11th int. model. conf.; 2015. p. 873–82. doi:10.3384/ecp15118873.
[15] Bonilla J, de la Calle A, Rodríguez-García MM, Roca L, Valenzuela L. Study on shell-and-tube heat exchanger models with different degree of complexity for process simulation and control design. Appl Therm Eng 2017;124:1425–40. https://doi.org/10.1016/j.applthermaleng.2017.06.129.
[16] Flueckiger SM, Iverson BD, Garimella SV, Pacheco JE. System-level simulation of a solar power tower plant with thermocline thermal energy storage. Appl Energy 2014;113:86–96. https://doi.org/10.1016/j.apenergy.2013.07.004.
[17] Hernández Arriaga I, Zaversky F, Astrain D. Object-oriented modeling of molten-salt-based thermocline thermal energy storage for the transient performance simulation of solar thermal power plants. Energy Procedia 2015;69:879–90. https://doi.org/10.1016/j.egypro.2015.03.116.
[18] Vasallo MJ, Bravo JM. A MPC approach for optimal generation scheduling in CSP plants. Appl Energy 2016;165:357–70. https://doi.org/10.1016/j.apenergy.2015.12.092.
[19] Li X, Xu E, Song S, Wang X, Yuan G. Dynamic simulation of two-tank indirect thermal energy storage system with molten salt. Renew Energy 2017;113:1311–9. https://doi.org/10.1016/j.renene.2017.06.024.
[20] Li Q, Bai F, Yang B, Wang Z, El B, Liu S, et al. Dynamic simulation and experimental validation of an open air receiver and a thermal energy storage system for solar thermal power plant. Appl Energy 2016;178:281–93. https://doi.org/10.1016/j.apenergy.2016.06.056.
[21] Rea JE, Oshman CJ, Olsen ML, Hardin CL, Glatzmaier GC, Siegel NP, et al. Performance modeling and techno-economic analysis of a modular concentrated solar power tower with latent heat storage. Appl Energy 2018;217:143–52. https://doi.org/10.1016/J.APENERGY.2018.02.067.
[22] Cioccolanti L, Tascioni R, Arteconi A. Mathematical modelling of operation modes and performance evaluation of an innovative small-scale concentrated solar organic Rankine cycle plant. Appl Energy 2018;221:464–76. https://doi.org/10.1016/j.apenergy.2018.03.189.
[23] Zhao B, Cheng M, Liu C, Dai Z. System-level performance optimization of molten-salt packed-bed thermal energy storage for concentrating solar power. Appl Energy 2018;226:225–39. https://doi.org/10.1016/J.APENERGY.2018.05.081.
[24] Suojanen S, Hakkarainen E, Kettunen A, Kapela J, Paldanius J, Tuononen M, et al. Integration of concentrated solar power (CSP) and circulating fluidized bed (CFB) power plants – final results of the COMBO-CFB project. AIP Conf. Proc. 2016;110016. https://doi.org/10.1063/1.4984490.
[25] Suojanen S, Hakkarainen E, Tähtinen M, Sihvonen T. Modeling and analysis of process configurations for hybrid concentrated solar power and conventional steam power plants. Energy Convers Manag 2017:134. https://doi.org/10.1016/j.enconman.2016.12.029.
[26] Hakkarainen E, Tähtinen M. Dynamic modelling and simulation of linear Fresnel solar field model based on molten salt heat transfer fluid. AIP Conf. Proc. 2016;1734. https://doi.org/10.1063/1.4949161.
[27] Al-Maliki WAK, Alobaid F, Kez V, Epple B. Modelling and dynamic simulation of a parabolic trough power plant. J Process Control 2016;39:123–38. https://doi.org/10.1016/j.jprocont.2016.01.002.
[28] Hakkarainen E, Sihvonen T, Lappalainen J. Dynamic modelling and simulation of CSP plant based on supercritical carbon dioxide closed Brayton cycle. AIP Conf. Proc. 1850 2016;070004:1–8. https://doi.org/10.1063/1.4984418.
[29] Hakkarainen E, Sihvonen T, Lappalainen J. Dynamic simulation of two concentrated solar power concepts with supercritical CO2 Brayton cycle. In: Proc. 1st eur. semin. supercrit. CO2 power syst., 2016, p. 2–6.
[30] Serrano-López R, Fradera J, Cuesta-López S. Molten salts database for energy applications. Chem Eng Process Process Intensif 2013;73:87–102. https://doi.org/10.1016/j.cep.2013.07.008.
[31] Boerema N, Morrison G, Taylor R, Rosengarten G. Liquid sodium versus Hitec as a heat transfer fluid in solar thermal central receiver systems. Sol Energy 2012;86:2293–305. https://doi.org/10.1016/j.solener.2012.05.001.
[32] Ferri R, Cammi A, Mazzei D. Molten salt mixture properties in RELAP5 code for thermodynamic solar applications. Int J Therm Sci 2008;47:1676–87. https://doi.org/10.1016/j.ijthermalsci.2008.01.007.
[33] Davis CB. Implementation of Molten Salt Properties into RELAP5-3D/ATHENA. Idaho Natl Eng Environ Lab Bechtel BWXT Idaho, LLC; 2005.
[34] Rodríguez-García M-M, Herrador-Moreno M, Zarza Moya E. Lessons learnt during the design, construction and start-up phase of a molten salt testing facility. Appl Therm Eng 2014;62:520–8. https://doi.org/10.1016/j.applthermaleng.2013.09.040.
[35] Apros. Process simulation software; 2018. < http://www.apros.fi/en/ > (accessed April 17, 2018).
[36] Hänninen M. Solution of one-dimensional flow and heat transfer processes with difference method. Lappeenranta: University of Technology; 1989.

[37] Lappalainen J, Korvola T, Alopaeus V. Modelling and dynamic simulation of a large MSF plant using local phase equilibrium and simultaneous mass, momentum, and energy solver. Comput Chem Eng 2017;97:242–58. https://doi.org/10.1016/j.compchemeng.2016.11.039.
[38] Vasserman AA, Kazavchinskii YZ, Rabinovich VA. Thermophysical properties of air and air components; 1966.
[39] Vasserman AA, Rabinovich VA. Thermophysical properties of liquid air and its components; 1968.
[40] Wallis GB. One-dimensional Two-phase Flow. New York: McGraw-Hill; 1969.
[41] Zavoico AB. Solar power tower – Design basis document. Albuquerque; 2001.
[42] Marcus Y. The compressibility of molten salts. J Chem Thermodyn 2013;61:7–10. https://doi.org/10.1016/j.jct.2013.01.021.
[43] Solutia. Therminol VP-1 2014:1–5.
[44] Ransom VH, Wagner RJ, Trapp JA, Feinauer LR. RELAP5/MOD2 code manual. Code structure, system models and solution method, vol. 1; 1985.